

Department of Physics and Astronomy

University of Heidelberg

Diploma thesis
in Physics

submitted by
Martin Florian Bessner
born in Heidelberg, Germany

February 2012

**Study of the ratio of $D^0 \rightarrow K^+ \pi^-$
to $D^0 \rightarrow K^- \pi^+$ decays with the
LHCb detector**

This diploma thesis has been carried out by Martin Florian Bessner
at the
Physical Institute
under the supervision of
Prof. Dr. Ulrich Uwer

Abstract: Study of the ratio of $D^0 \rightarrow K^+\pi^-$ to $D^0 \rightarrow K^-\pi^+$ decays with the LHCb detector

In the Standard Model of particle physics, a D^0 meson can mix into a $\overline{D^0}$ and vice versa. The predicted mixing rate is very small, but processes of new physics beyond the Standard Model can significantly influence this rate. D^0 - $\overline{D^0}$ mixing can be observed via a measurement of the time-dependent ratio of $D^0 \rightarrow K^+\pi^-$ to $D^0 \rightarrow K^-\pi^+$ decays. In this work, a measurement of the time-integrated ratio of these decay channels is presented, using a dataset from the LHCb experiment which corresponds to an integrated luminosity of $\int \mathcal{L} dt = (36.4 \pm 3.6)\text{pb}^{-1}$. To identify the flavour of the D-meson, the strong decay $D^{*+} \rightarrow D^0\pi_s^+$ is used. The analysis uses D^{*+} mesons from the proton-proton interaction vertex. The different background components and their influence on the measurement are discussed.

An important background for the time-dependent measurement of the ratio are D^0 from non-prompt D^{*+} decays, where the D^{*+} mesons originate from B meson decays. For these events the decay time estimation of the D^0 is wrong. Using semileptonic $\overline{B^0} \rightarrow D^{*+}\mu\nu_\mu X$ decays, the decay time distribution of D^0 from non-prompt D^{*+} is studied. A method is developed to account for this background in the mixing analysis.

Kurzfassung: Studie des Verhältnisses von $D^0 \rightarrow K^+\pi^-$ zu $D^0 \rightarrow K^-\pi^+$ Zerfällen mit dem LHCb Detector

Im Standardmodell der Teilchenphysik kann ein D^0 -Meson in ein $\overline{D^0}$ übergehen und umgekehrt. Die vorhergesagte Mischungsrate ist sehr klein, jedoch könnten Prozesse neuer Physik jenseits des Standardmodells diese Rate wesentlich beeinflussen. D^0 - $\overline{D^0}$ -Mischung kann mithilfe der Messung der zeitabhängigen Rate von $D^0 \rightarrow K^+\pi^-$ zu $D^0 \rightarrow K^-\pi^+$ Zerfällen gemessen werden. In dieser Arbeit wird eine Messung des über die Zeit integrierten Verhältnisses dieser Zerfallskanäle vorgestellt. Dabei wird ein Datensatz des LHCb-Experiments verwendet, der einer integrierten Luminosität von $\int \mathcal{L} dt = (36.4 \pm 3.6)\text{pb}^{-1}$ entspricht. Um die Quark-Zusammensetzung bei der Produktion zu bestimmen, wird der Zerfall $D^{*+} \rightarrow D^0\pi_s^+$ über die starke Wechselwirkung benutzt. Die Analyse nutzt D^{*+} -Mesonen, die vom Proton-Proton-Kollisionspunkt stammen. Die verschiedenen Untergrundkomponenten und ihr Einfluss auf die Messung werden diskutiert.

Ein wichtiger Untergrund in der zeitabhängigen Messung des Verhältnisses der Zerfälle sind D^0 von D^{*+} , die beim Zerfall von B-Mesonen entstehen. Für diese Ereignisse ist die Abschätzung der Zerfallszeit falsch. Mit semileptonischen Zerfällen $\overline{B^0} \rightarrow D^{*+}\mu\nu_\mu X$ wird die Verteilung der Zerfallszeiten der D^0 aus diesen D^{*+} untersucht. Eine Methode, um ihren Einfluss auf die Messung zu berücksichtigen, wird entwickelt.

Contents

1	Introduction	9
2	Theory	11
2.1	Neutral D meson system	11
2.2	$D^0 \rightarrow K \pi$ decays	12
2.3	Related measurements	13
3	LHCb Detector	15
3.1	Detector concept	15
3.2	Subdetectors	16
3.2.1	VELO	16
3.2.2	Tracking system	16
3.2.3	RICH detectors	18
3.2.4	Calorimeters	18
3.2.5	Muon system	19
4	Data selection and background composition	21
4.1	General	21
4.2	Simulation and event reconstruction	21
4.3	Background contributions	22
4.3.1	Random slow pions	22
4.3.2	Combinatorial background	23
4.3.3	Misreconstructed D^0	23
4.3.4	Reflections, misidentification	23
4.3.5	D^0 mesons created in non-prompt D^* decays	24
4.4	Data selection	24
4.4.1	Trigger	25
4.4.2	Track momenta	26
4.4.3	Track and vertex fit quality	26
4.4.4	Particle identification	27

4.4.5	Impact parameter	27
4.4.6	Flight distance	28
4.4.7	D^0 topology	28
5	Measurement method	31
5.1	Extraction of mixing parameters	31
5.2	Signal yield determination	32
5.2.1	Signal shape	33
5.2.2	Random slow pion background shape	34
5.2.3	Combinatorial background shape	34
5.2.4	Misreconstructed background shape	34
5.2.5	Fitting method	34
5.2.6	Alternative method	35
5.3	Double misidentified events	35
5.3.1	Mass exchange method	35
5.3.2	Misidentified events included in fit	38
5.4	Asymmetries	38
5.4.1	Production asymmetry	38
5.4.2	Slow pion detection asymmetry	39
5.4.3	D^0 daughter detection asymmetry	40
5.4.4	Magnet polarity and spatial asymmetry	40
6	Background from non-prompt D^0	43
6.1	Introduction	43
6.2	Impact parameter fit	44
6.3	Reconstruction of non-prompt D^0	46
6.3.1	Suitable B hadron decay channels	46
6.3.2	Selection of $B \rightarrow D^* \mu \nu$ (X)	46
6.3.3	Comparison to simulation	47
6.3.4	Application to data	50
6.3.5	Result	51
6.3.6	Correction of the bias on mixing parameters	52
7	Time-integrated ratio	61
7.1	Modified fit method	61
7.2	Systematic uncertainties	64
7.2.1	Double misidentification	65
7.3	Lifetime acceptance correction	66
7.4	Results	68
8	Summary and Outlook	69
8.1	Summary	69
8.2	Outlook	70
8.2.1	Toy MC study	70

8.2.2	Possible future measurements	72
A	Appendix	79
A.1	Double misidentified events	79
A.2	Detection and production asymmetries	80
A.3	Influence of non-prompt D^0 on the WS to RS ratio	81
	Bibliography	83
	Acknowledgments	87

Introduction

The Large Hadron Collider (LHC), built at CERN in Geneva, is the world's largest and highest-energetic particle accelerator. In the LHC, proton beams with an energy of 3.5 TeV per proton are collided in four main detectors: ATLAS, CMS, ALICE and LHCb. The first collisions took place in 2009, with regular operation since 2010.

The primary target of the LHC detectors is the search for new physics beyond the standard model of particle physics (Standard Model), together with precision measurements of parameters of the Standard Model. If existing, it is expected that the Higgs boson can be found. Lead-lead collisions are studied with the ALICE detector.

The Standard Model is well established. Up to now, no striking violation from its predictions was found by particle physics experiments.

However, it is known that the Standard Model is incomplete, as it has theoretical limits for high energies and it cannot describe experimental results from cosmology such as the size of the matter-antimatter asymmetry or the nature of dark matter. In addition, it does not include gravity.

Therefore, it is expected that new physics beyond the Standard Model exists. There are two different approaches to search for possible new effects, both are pursued at the LHC detectors: In the first approach one searches for the production of new particles by reconstructing them using their decay products. ATLAS and CMS focus on this direct method to probe new effects. The other possibility is to perform precision measurements of decay properties of already known particles such as B and D mesons. For these decays, new physics can alter the decay properties significantly.

LHCb is specialised to perform such measurements. The LHCb detector is a single arm forward spectrometer in the pseudo-rapidity region of $2 < \eta < 5$ ¹, designed to analyse the production and decay of mesons with a bottom quark (B-mesons) or a charm-quark (D-mesons). B and D mesons are abundantly pro-

¹The pseudo-rapidity η is defined as $\eta = -\log(\tan\frac{\theta}{2})$ with the polar angle θ .

duced in proton-proton collisions, which allows to study them with high precision.

Neutral D^0 mesons consist of a charm-quark and an anti-up quark and can oscillate into their own antiparticles, \overline{D}^0 . Mixing of neutral mesons was first found in the system of neutral kaons and later in the B-meson system. The D^0 meson² is unique as it is the only meson built from up-type quarks where mixing can be observed. The Standard Model predicts a small mixing probability, which makes its observation very difficult. New particles which contribute to the quantum corrections could significantly increase the mixing probability. Mixing in the charm system has been discovered, with the no-mixing hypothesis excluded at a level of 10 standard deviations in the combination of measurements from CDF [1], BELLE [2] and BABAR [3]. However, no single measurement exceeded a significance of 5 standard deviations yet. It is expected that LHCb can reach this sensitivity with the dataset taken in 2011.

To observe mixing of D^0 mesons, the flavour of the particle (D^0 or \overline{D}^0) at production and at decay time has to be measured. While the flavour at the time of the decay is usually determined from flavour specific decay modes such as $D^0 \rightarrow K^- \pi^+$ where the charges of the decay particles determine the D^0 flavour, the flavour at production is determined by only using D^0 from the decay chain $D^{*+} \rightarrow D^0 \pi_s^+$. Here the charge of the pion π_s from the D^{*+} identifies the D^0 flavour at production. The most common D^0 decay is called right sign (RS) decay and corresponds to a D^0 which has not mixed: $D^0 \rightarrow K^- \pi^+$. If the D^0 mixes to \overline{D}^0 , a wrong sign (WS) decay occurs: $D^0 \rightarrow \overline{D}^0 \rightarrow K^+ \pi^-$. In this case the kaon (K^+) from the D^0 and the pion π_s^+ from the D^{*+} have the same charge. In addition to the mixing there is also the doubly Cabibbo suppressed (DCS) decay $D^0 \rightarrow K^+ \pi^-$ which also leads to the same charge for kaon and π_s . The fraction of the D^0 which mix and decay via the DCS decay channel afterwards can be neglected.

The sum of WS decays via DCS, via mixing and via the interference of both lead to a decay rate of about 0.4% of the RS rate. To observe mixing, the three contributions leading to a WS decay have to be separated. This can be done by measuring the time-dependent rate of WS to RS decays.

In chapter 2, the D^0 - \overline{D}^0 system is presented. A brief overview over the LHCb detector is given in chapter 3. The data selection and the background contributions in the analysis are shown in chapter 4. Chapter 5 explains the strategy to measure WS decays and D^0 mixing. Chapter 6 shows a specific type of background events which arises in the time-dependent mixing analysis and presents a new method to treat biases coming from this background component. In chapter 7, the measurement of a time-integrated measurement of the WS to RS ratio is presented.

²Unless stated otherwise, charge conjugated modes are always implied

Theory

2.1 Neutral D meson system

A D^0 meson consists of a charm quark and an anti-up quark. While the production of D^0 can proceed via strong and weak interaction, they decay only weakly. They can oscillate into their own antiparticles via box diagrams and long-range contributions with intermediate particles like $D^0 \rightarrow KK \rightarrow \bar{D}^0$, both options are shown in figure 2.1.



Figure 2.1: Sketch of the contributions to D^0 mixing: Box diagram (left) and long-range contributions with intermediate states like KK , $\pi\pi$ or $K\pi$ (right)

The time-evolution of the D^0 is usually described by an effective Hamiltonian $\mathcal{H}_{eff} = M - \frac{i}{2}\Gamma$, where M and Γ are 2 x 2 Hermitian matrices:

$$M = \begin{pmatrix} M_{11} & M_{12} \\ M_{21} & M_{22} \end{pmatrix} \quad (2.1)$$

and

$$\Gamma = \begin{pmatrix} \Gamma_{11} & \Gamma_{12} \\ \Gamma_{21} & \Gamma_{22} \end{pmatrix} \quad (2.2)$$

The time-evolution is then given by

$$i \frac{\partial}{\partial t} \begin{pmatrix} D^0 \\ \bar{D}^0 \end{pmatrix} = \mathcal{H}_{eff} \begin{pmatrix} D^0 \\ \bar{D}^0 \end{pmatrix} \quad (2.3)$$

Assuming CPT symmetry one obtains $m(D^0) = m(\overline{D^0})$ and $\Gamma(D^0) = \Gamma(\overline{D^0})$, which corresponds to $M_{11} = M_{22}$ and $\Gamma_{11} = \Gamma_{22}$. If in addition, the system is invariant under CP transformation, all matrix elements of M and Γ are real and therefore $M_{12} = M_{21}$ and $\Gamma_{12} = \Gamma_{21}$.

The diagonalization leads to eigenstates D_1 and D_2 which are linear combinations of D^0 and $\overline{D^0}$:

$$|D_1\rangle = p |D^0\rangle + q |\overline{D^0}\rangle \text{ and } |D_2\rangle = p |D^0\rangle - q |\overline{D^0}\rangle,$$

where the coefficients p and q are complex and satisfy the normalisation condition $|p|^2 + |q|^2 = 1$.

The ratio $\frac{p}{q}$ can be calculated from the matrix elements of M and Γ via

$$\frac{p}{q} = \sqrt{\frac{2M_{12}^* - i\Gamma_{12}^*}{2M_{12} - i\Gamma_{12}}} \quad (2.4)$$

In the absence of CP violation, $M_{12}^* = M_{12}$ and $\Gamma_{12}^* = \Gamma_{12}$ lead to $\frac{p}{q} = 1$. Otherwise, the rates of $D^0 \rightarrow \overline{D^0}$ and $\overline{D^0} \rightarrow D^0$ mixing are different.

D_1 and D_2 have different masses M_1 and M_2 and decay widths Γ_1 and Γ_2 . With the average $\Gamma = \frac{\Gamma_1 + \Gamma_2}{2}$, it is possible to define dimensionless mixing parameters

$$x = \frac{M_1 - M_2}{\Gamma} \quad (2.5)$$

and

$$y = \frac{\Gamma_1 - \Gamma_2}{2\Gamma} \quad (2.6)$$

The eigenvalues of $D_{1,2}$ with respect to \mathcal{H}_{eff} are $\lambda_{1,2} = M_{1,2} \pm i\Gamma_{1,2}$, which leads to the time-evolution $|D_{1,2}(t)\rangle = e^{-i\lambda_{1,2}t} |D_{1,2}(0)\rangle$.

The probability to find a neutral D meson which is produced in state D^0 at $t = 0$ as D^0 after time t is given by

$$P(D^0 \rightarrow D^0, t) = |\langle D^0 | D^0(t)\rangle|^2 = \frac{e^{-\Gamma t}}{2} (\cosh(y\Gamma t) + \cos(x\Gamma t)) \quad (2.7)$$

and the probability to find the meson in state $\overline{D^0}$ is given by

$$P(D^0 \rightarrow \overline{D^0}, t) = |\langle \overline{D^0} | D^0(t)\rangle|^2 = \frac{e^{-\Gamma t}}{2} \left|\frac{p}{q}\right|^2 (\cosh(y\Gamma t) - \cos(x\Gamma t)) \quad (2.8)$$

2.2 $D^0 \rightarrow K \pi$ decays

Two D^0 decay channels are considered in this analysis: The decay $D^0 \rightarrow K^- \pi^+$ is denoted as right sign (RS) decay and the strongly suppressed decay $D^0 \rightarrow K^+ \pi^-$, which is usually called wrong sign (WS) decay. Feynman graphs of the decays are shown in figure 2.2.

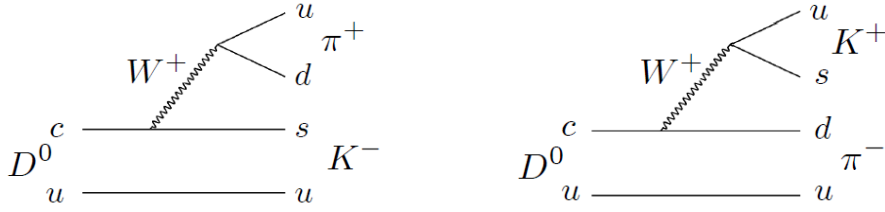


Figure 2.2: Feynman graphs of RS (left) and WS (right) decays of $D^0 \rightarrow K^\pm \pi^\mp$

The RS decay has a branching fraction of $\approx 3.9\%$, whereas the branching fraction of the WS decay is only $\approx 0.015\%$ [4]. The difference comes from the Cabibbo suppression of the transitions between quarks of different families, as the CKM matrix elements V_{cd} and V_{us} are much smaller than V_{cs} and V_{ud} . Hence, this decay is called "doubly Cabibbo suppressed" or short DCS decay.

CP violation in the charm system is very small and can be neglected in the analysis of WS events with the current size of the available datasets.

DCS decays, mixing and the interference between mixing and DCS decays lead to three sources of WS decays. In general, a strong phase difference δ between the amplitudes of the first two processes can occur. To account for this, modified mixing parameters x', y' are introduced with $x' = x \cos(\delta) + y \sin(\delta)$ and $y' = -x \sin(\delta) + y \cos(\delta)$. $\cos(\delta)$ is close to 1, as measured by the CLEO collaboration [5]: $\cos(\delta) = 1.03_{-0.17}^{+0.31}(\text{stat}) \pm 0.06(\text{sys})$. This implies a high correlation between x' and x and between y' and y .

With the approximation of $x', y' \ll 1$, the probability that a D^0 produced at time $t = 0$ decays via the RS channel at time t is given by $RS(t) \propto e^{-\Gamma t}$, while the probability of a WS decay is [6]

$$WS(t) \propto e^{-\Gamma t} \left(R_D + \sqrt{R_D} y' \cdot \Gamma t + \frac{x'^2 + y'^2}{4} \cdot (\Gamma t)^2 \right) \quad (2.9)$$

where R_D is the ratio of DCS to RS decays without mixing.

This leads to the ratio of WS to RS decays:

$$\frac{WS(t)}{RS(t)} = M(t) = R_D + \sqrt{R_D} y' \cdot \Gamma t + \frac{x'^2 + y'^2}{4} \cdot (\Gamma t)^2 \quad (2.10)$$

It is not possible to determine the sign of x' with the analysis of WS events, as the measurement is only sensitive to x'^2 .

2.3 Related measurements

Together with the singly cabibbo suppressed decay $D^0 \rightarrow K^+ K^-$, it is possible to construct other observables. These can help to constrain more parameters of

charm mixing like p and q or the sign of x' , and the consistency between the different measurements in the charm system is a test of the Standard Model.

R_m gets defined as $\left|\frac{q}{p}\right|$ and the phase ϕ is defined as $\phi = \arg\left(\frac{q}{p}\right)$, similar to [6].

The effective lifetime of $D^0 \rightarrow K^+K^-$ is then given by

$$\Gamma(D^0 \rightarrow KK) = \Gamma(1 + R_m(y \cos(\phi) - x \sin(\phi))) \quad (2.11)$$

while the decay rate of $\bar{D}^0 \rightarrow K^+K^-$ is

$$\Gamma(\bar{D}^0 \rightarrow KK) = \Gamma(1 + R_m^{-1}(y \cos(\phi) + x \sin(\phi))) \quad (2.12)$$

Using previous experimental results that $R_m \approx 1$, it is possible to define A_m as the approximation $R_m^{\pm 2} = 1 \pm A_m$. This allows to measure the following two quantities [6]:

$$A_\Gamma = \frac{\Gamma(D^0 \rightarrow K^+K^-) - \Gamma(\bar{D}^0 \rightarrow K^+K^-)}{\Gamma(D^0 \rightarrow K^+K^-) + \Gamma(\bar{D}^0 \rightarrow K^+K^-)} \approx \frac{1}{2}A_m y \cos(\phi) - x \sin(\phi) \quad (2.13)$$

$$y_{cp} = \frac{\Gamma(D^0 \rightarrow K^+K^-)}{\Gamma(D^0 \rightarrow K^-\pi^+)} - 1 = y \cos(\phi) - x \sin(\phi) \frac{A_m}{2} \quad (2.14)$$

As the LHC is a proton-proton collider, the colliding particles are not invariant under charge conjugation. Therefore, the number of produced D^0 and \bar{D}^0 might be different. The D^0 production asymmetry $A_{prod} = \frac{N(D^0) - N(\bar{D}^0)}{N(D^0) + N(\bar{D}^0)}$ influences the measurement of y_{cp} :

$$y_{cp} = y \cos(\phi) - x \sin(\phi) \left(\frac{A_m}{2} + A_{prod} \right) \quad (2.15)$$

A non-zero A_Γ would be a direct sign of CP-violation, and a significant difference between y_{cp} and y' can be a hint for CP-violation, too [6].

With the second singly Cabibbo suppressed decay channel $D^0 \rightarrow \pi^+\pi^-$, another observable can be constructed:

$$\Delta A_{CP} = \frac{N(D^0 \rightarrow K^+K^-) - N(\bar{D}^0 \rightarrow K^+K^-)}{N(D^0 \rightarrow K^+K^-) + N(\bar{D}^0 \rightarrow K^+K^-)} - \frac{N(D^0 \rightarrow \pi^+\pi^-) - N(\bar{D}^0 \rightarrow \pi^+\pi^-)}{N(D^0 \rightarrow \pi^+\pi^-) + N(\bar{D}^0 \rightarrow \pi^+\pi^-)} \quad (2.16)$$

While it was expected [7] that this quantity is at the permille level or less, a recent LHCb measurement [8] shows a deviation of 3.5 standard deviations from this prediction:

$$\Delta A_{CP} = -0.82 \pm 0.21(\text{stat}) \pm 0.11(\text{sys}) \quad (2.17)$$

Further measurements in the charm sector can help to understand the nature of this difference and decide whether it can be explained within the Standard Model or whether it is a sign of new physics beyond the description of the Standard Model.

LHCb Detector

3.1 Detector concept

The LHCb detector is designed to study the production and decay of mesons with a bottom quark (B mesons) and a charm quark (D mesons) produced in proton-proton collisions with a center of mass energy of 14 TeV. The design luminosity foreseen for the LHCb is $\mathcal{L} = 2 \cdot 10^{32} \text{cm}^{-2} \text{s}^{-1}$ with an expected integrated luminosity of $\int \mathcal{L} dt = 2 \text{fb}^{-1}$ per year. With the LHC design value of 25 ns proton bunch spacing and a cross section of $\approx 60 \text{mb}$ for events visible in the detector, this corresponds to about 0.4 visible interactions per bunch crossing. During the data taking periods under study, the bunch spacing was 50-100 ns, and the center of mass energy was 7 TeV. The number of interactions per bunch crossing was increased such that the detector was operated at a luminosity of up to $\mathcal{L} = 4 \cdot 10^{32} \text{cm}^{-2} \text{s}^{-1}$ at LHCb. This is two-times larger than originally foreseen, despite the lower number of colliding bunches.

B and D mesons produced in the proton-proton collisions tend to fly along the beam axis. The two-dimensional distribution of their polar angles is shown in figure 3.1. Therefore, the detector is built around the beam axis, with a coverage of 10-300 mrad around it in horizontal direction (x-axis) and 10-250 mrad in vertical direction (y-axis). The z-direction is along the beam axis, with its origin near the proton-proton collision point. The larger acceptance in x-direction accounts for the dipole magnet which bends particles in the x-z-plane.

In order to analyze B and D mesons, a good track reconstruction and particle identification is required. Therefore, LHCb consists of several subdetectors, which are shown in figure 3.2. Their designs and purposes are explained in the following section.

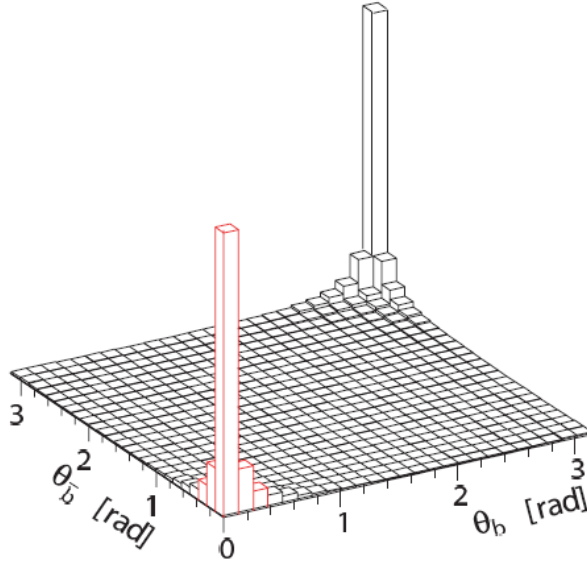


Figure 3.1: *Two-dimensional angular distribution of $b\bar{b}$ mesons produced in the proton-proton collisions, taken from [9]. The LHCb detector acceptance covers the red region.*

3.2 Subdetectors

3.2.1 VELO

The *VErtex LOcator* (VELO) is built around the interaction region of the proton-proton collisions. It is a silicon strip detector with 21 layers. Its primary target is to reconstruct the primary vertex of collisions together with secondary vertices from particle decays. This allows to detect short-lived particles via their flight-length.

In order to improve the resolution, it is built as close as possible to the beam, with the innermost parts only 5 mm away from the beam axis. To protect the sensors, the VELO consists of two movable halves: They are retracted until the beam is stable enough to move the VELO in.

The resolution of the primary vertex is $60 \mu\text{m}$ in z -direction and $10 \mu\text{m}$ in transversal direction. Depending on the decay topology and the decay kinematics this resolution leads to a resolution of the measured decay time of typically 50 fs. Reference [10] contains more information about the VELO.

3.2.2 Tracking system

The tracking system consists of the VELO, the *Trigger Tracker* (TT) and the combination of *Inner Tracker* (IT) and *Outer Tracker* (OT). All parts can mea-

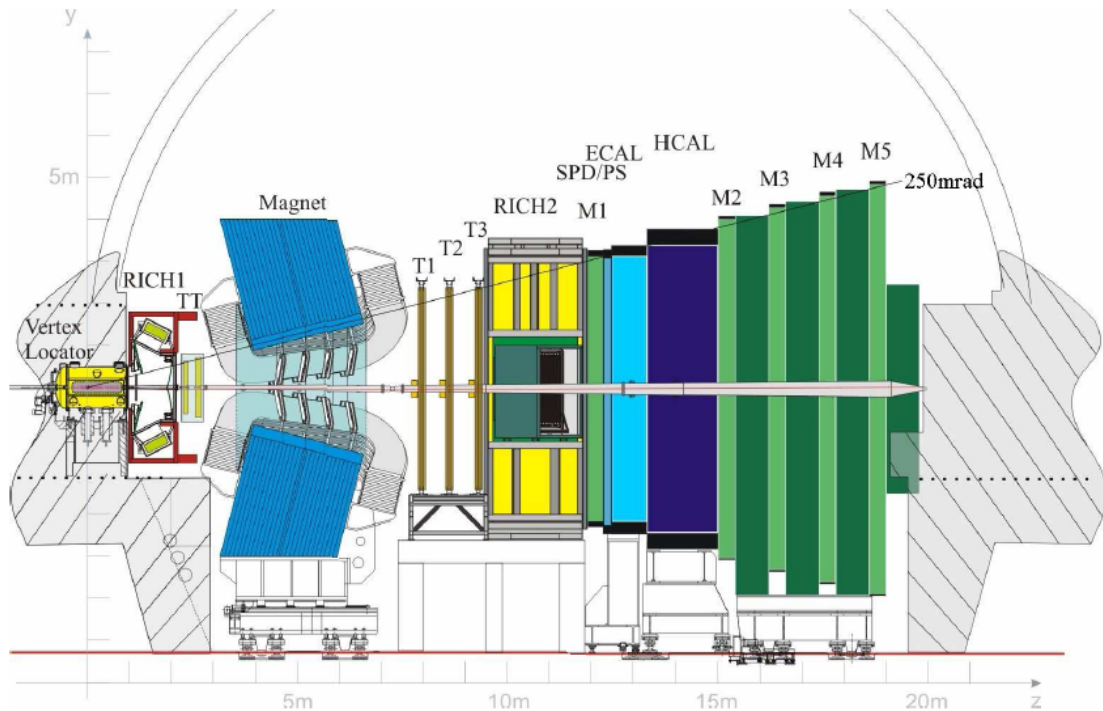


Figure 3.2: Overview over the LHCb detector [11]. The interaction point is on the left side, detectable particles fly towards the right side. The individual subdetectors are described in section 3.2.

sure the tracks of charged particles, and the combined data from these subdetectors provide a way to determine the particle paths through the whole tracking system.

A dipole magnet between TT and IT/OT provides an integrated magnetic flux of $\int B dl = 4.2 \text{ Tm}$ along the beam axis. Together with the tracking detectors, the magnetic field offers the possibility to measure the particle momentum using the bending of the charged particles inside the magnetic field. The field is aligned with the y-coordinate, therefore particles are bent in the x-z-plane. The magnet polarity can be switched. In order to determine the momentum of particles, the measurements of the x-positions within the detectors need a high precision.

The TT in front of the magnet is a silicon strip detector consisting of two structures, each with two stereo-layers. One stereo layer measures the x-position, and the other layer is rotated by 5° in the x-y-plane. This allows to measure the y-coordinate too, albeit with a lower precision. The resolution in x-direction is $\approx 60 \mu\text{m}$. See [12] for more information.

The IT and OT are located behind the dipole magnet. The IT is located close to the beam pipe in the region of high particle flux. It is a silicon strip detector. The OT surrounds the IT and is made out of straw tube detectors. It has 3

stations (T1 to T3) with four stereo-layers each. For more details about the IT and OT, see [13] and [14].

3.2.3 RICH detectors

In a medium, the speed of light is modified by the refractive index $n = \frac{c}{c_n}$ with the light velocity c_n in the medium. Charged particles which traverse the medium faster than the speed of light can emit photons under an angle θ relative to the particle momentum, with $\cos(\theta) = \frac{v_p}{v} = \frac{1}{n\beta}$, where v is the velocity of the particle and $\beta = \frac{v}{c}$. The emitted Cherenkov photons form a cone around the particle track with opening angle θ .

In *Ring Imaging CHerenkov* (RICH) detectors, the Cherenkov photons are projected to a plane of photosensors such that all photons from a single particle form a ring. The diameter is given by the Cherenkov angle and the detector geometry, therefore θ can be measured and β can be calculated. Together with the momentum measurement from the tracking system, it is possible to evaluate the mass and therefore the type of the particle. This allows to distinguish between electrons, pions, kaons and protons.

Two RICH detectors are used at LHCb: RICH1 is located between VELO and TT, and RICH2 is installed behind IT/OT. RICH1 uses an aerogel and C_4F_{10} as radiator materials, it is designed for low-energetic particles in the range of 1 to 50 GeV. RICH2 uses the less dense CF_4 and is designed for particles with an energy between 15 and 100 GeV. Reference [15] provides more information about the RICH design.

3.2.4 Calorimeters

The calorimeter system provides an energy measurement for electrons and photons but also for charged and uncharged hadrons. This is especially important for the trigger system (see section 4.4.1), as the calorimeters can detect particles with a high transverse momentum. Incoming particles interact with the material of the calorimeters and produce showers which can be detected by scintillators.

The first part is the Scintillating Pad Detector (SPD). It is followed by 1 cm of lead, the *PreShower* Detector (PS) and the *Electromagnetic CALorimeter* (ECAL). Showers from photons and electrons are detected here. The ECAL is a shashlik calorimeter with material equivalent to 25 electromagnetic interaction lengths and 1.1 hadronic interaction length. It has a relative energy resolution of $\frac{\sigma E}{E} = \frac{9.5\%}{\sqrt{E/GeV}} \oplus 0.8\%$, where \oplus means quadratic summation. The SPD can distinguish electrons and photons, as it detects electrons but not photons.

The *Hadronic CALorimeter* (HCAL) is located behind the ECAL and designed to detect hadronic showers. It covers 5.6 hadronic interaction lengths and has an energy resolution of $\frac{\sigma E}{E} = \frac{69\%}{\sqrt{E/GeV}} \oplus 9\%$. The main purpose of the HCAL

is to provide a fast trigger signal for high-energetic hadrons. For more details, see [16].

3.2.5 Muon system

The muon system consists of 5 chambers, one chamber (M1) in front of the calorimeters and four (M2 to M5) behind it. They are built as *MultiWire Proportional Chambers* (MWPC). Near the beam pipe detectors built from *Gas Electron Multipliers* (GEM) are used to handle the higher rate of particles. M2 to M5 are separated by 80 cm of iron. These iron absorbers stop hadrons which passed the calorimeters. Behind the last muon station, there is an additional iron absorber to shield the detector from particles coming from the other side. The muon detectors provide a fast trigger signal for muons. More details about the muon system can be found in [17].

Data selection and background composition

4.1 General

Data suitable for the analysis of D^0 - \overline{D}^0 mixing were taken during two data taking periods: In 2010, a dataset corresponding to an integrated luminosity of $\int \mathcal{L} dt = (36.4 \pm 3.6) \text{pb}^{-1}$ was collected, while in 2011 LHCb recorded a dataset corresponding to $\int \mathcal{L} dt = (1024 \pm 100) \text{pb}^{-1}$. After applying a selection for events containing the signal decay channel $D^{*+} \rightarrow D^0(\rightarrow K\pi)\pi_s^+$, this results in approximately $3 \cdot 10^5$ signal candidates in 2010 and $1.1 \cdot 10^7$ signal candidates in 2011. Different trigger settings have been used in 2010 and 2011, therefore the datasets do not scale and cannot be combined. They are used as two independent sets for different analyses instead.

4.2 Simulation and event reconstruction

The simulation of proton-proton collisions and the detector response to the corresponding events is crucial for the understanding of the LHCb detector. Simulated events provide a way to check many aspects of analyses, as the underlying simulated physics is known.

At LHCb, simulation is done with the software package GAUSS [18]. It combines several programs which are necessary to simulate events: The event generator PYTHIA [19] simulates the proton-proton collisions. B- and D-mesons are then processed by EvtGen [20], which handles the decays of these particles. Both programs simulate the physical processes. They can be adjusted to produce effects which are not yet observed, for example new particles or decay channels which are searched for at LHCb. Afterwards, GEANT4 [21] calculates the propagation of the particles through the detector, this includes effects from the magnetic field and material interaction. As last step, Boole [22] evaluates the detector response

to the particles and determines which channels of the various LHCb subdetectors are hit.

The result are simulated events which have the same format as data from the real detector. In addition, the simulated events contain information about the simulated physical processes: It is possible to read out which particles generated the simulated detector response in each event.

The event reconstruction is performed with Brunel [23], which forms particle tracks and clusters out of individual hits in the detector. In addition, particle identification is done, mainly based on data from the RICH subdetectors (see section 3.2.3). The LHCb detector cannot measure the energy of the particles directly with high precision. Therefore, the energy is calculated from the momentum of detected tracks with hypotheses about the particle mass. By adding the relativistic 4-momenta of two or more particles, it is possible to construct a possible decay of a particle and to calculate its 4-momentum, decay vertex and invariant mass. The software DaVinci [23] uses the full event data to reconstruct particles and performs a fit to the reconstructed physics scenario with all involved particles. This gives access to the properties of the decaying particles like their mass, their momentum or their production and decay vertex.

4.3 Background contributions

In order to find D^{*+} signal candidates, reconstructed kaons and pions are combined to form a D^0 , which is combined with another pion to build a D^{*+} . This pion is called "slow" or "soft" pion π_s , as it has a low average momentum. The mass of the D^0 and the D^{*+} are calculated by adding up the 4-momenta of its daughter particles. To distinguish between signal and background particles, the reconstructed D^0 mass m_{D^0} and the reconstructed mass difference between D^0 and D^{*+} , $\delta m = m_{D^{*+}} - m_{D^0}$ are used. In the two-dimensional plane of these variables, signal and most background types separate. Figure 4.1 shows the D^0 mass and δm for the RS and WS signal candidates. A fit to the data is described in chapter 5, and projections of the two-dimensional distributions are shown in figure 5.1. Several types of background arise from this method:

4.3.1 Random slow pions

A correctly identified D^0 can be combined with an uncorrelated pion π , mainly from the primary vertex. The resulting candidates have a peak in the D^0 mass, while in δm they have a broad distribution as there is no correlation between the D^0 and the π . This is the main background contribution for WS signal candidates. In figure 4.1, this background is located in regions 2 and 4.

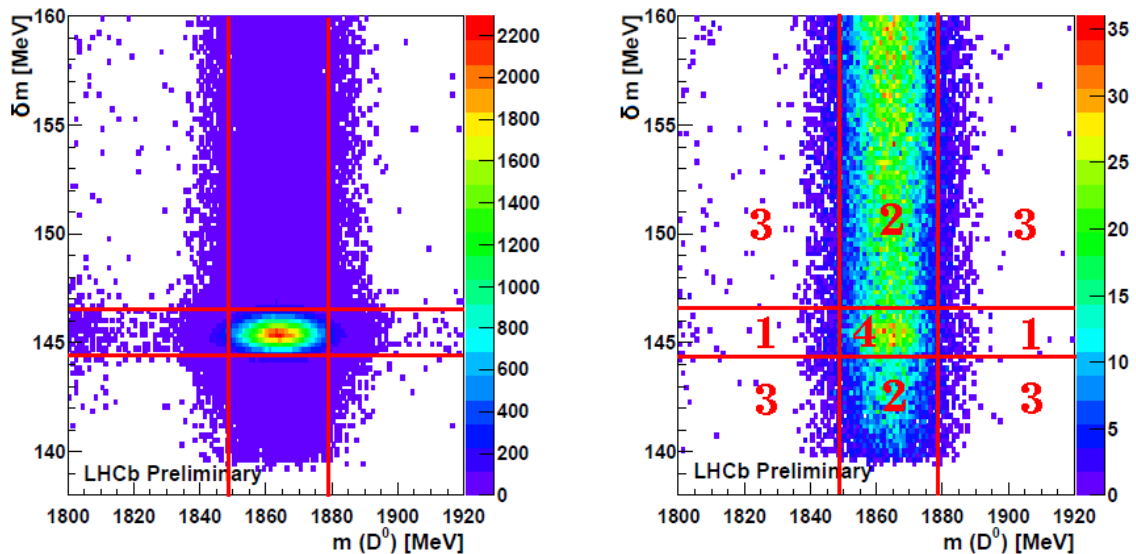


Figure 4.1: Two-dimensional distribution of RS (left) and WS (right) events in the $m(D^0)$, δm plane. The red lines and numbers show the different regions, as described in section 4.3. They are the same for RS and WS events.

4.3.2 Combinatorial background

Uncorrelated kaons and pions can get combined to a D^0 candidate. As there is no real D^0 , the added slow pion is from combinatorial background as well. This background has a broad distribution over the two-dimensional signal plane and can be found in all regions in figure 4.1.

4.3.3 Misreconstructed D^0

A D^0 from D^{*+} can decay into final states with additional particles X , $D^0 \rightarrow K^\pm \pi^\mp X$, where the kaon and the pion of the decay products are combined to a D^0 and other decay products X are not reconstructed. This gives lower D^0 masses in the reconstruction, whereas δm is not affected in first order. In figure 4.1, these events can be found in region 4 and in the left part of region 1.

The most important channels are $D^0 \rightarrow K^\pm \pi^\mp \pi^0$ and radiative events, where the D^0 decay or interaction with matter produces one or more photons.

4.3.4 Reflections, misidentification

The RICH subdetectors (see section 3.2.3) provide a good particle identification. However, some pions can be identified as kaons and vice versa, so $D^0 \rightarrow KK$ and $D^0 \rightarrow \pi\pi$ can be reconstructed as $D^0 \rightarrow K\pi$. This effect is called reflection and

the reconstructed D^0 has a mass which is shifted by approximately 100 MeV, where the the magnitude of the shift depends on the kinematics of the decay and the direction depends on the type of misidentification. $D^0 \rightarrow K^- K^+$ misidentified as $D^0 \rightarrow K^\pm \pi^\mp$ have a smaller reconstructed mass, while $D^0 \rightarrow \pi^- \pi^+$ misidentified as $D^0 \rightarrow K^\pm \pi^\mp$ have a larger reconstructed mass.

In addition, in a $D^0 \rightarrow K^\pm \pi^\mp$ decay, both decay products can be misidentified at the same time, giving a fake WS $D^0 \rightarrow K^+ \pi^-$ candidate from a real RS $D^0 \rightarrow K^- \pi^+$ decay. This has to be taken into account, as the large RS signal can contribute to the much smaller WS signal, while the opposite direction is negligible. Section 5.3 gives a more detailed discussion of this type of background.

These background types are located in region 4 and 1 in figure 4.1.

4.3.5 D^0 mesons created in non-prompt D^* decays

Most D^{*+} originate from the primary vertex, but some of them are produced in decays of B-mesons (non-prompt D^{*+}). Since B-mesons have a typical lifetime of about 1.5 ps, their decay and the D^{*+} production is displaced from the primary vertex. The reconstruction and decay time measurement assumes that all D^{*+} come from the primary vertex. This is wrong for D^0 mesons from non-prompt D^{*+} decays (non-prompt D^0), leading to a wrong reconstructed D^0 decay time, as shown in figure 4.2. Non-prompt D^0 are from real D^{*+} , therefore they have a D^0 mass and δm like signal events and cannot be distinguished from signal events with these variables. Non-prompt D^0 do not influence time-integrated measurements as the decay time is not used there, but in time-dependent measurements this effect has to be considered as background source.

In chapter 6, a new method to analyse and treat the non-prompt D^0 background is presented.

4.4 Data selection

Collisions in the LHC took place with a rate of 10 to 20 MHz during the analyzed data taking periods. To reduce the data rate, a trigger system filters the events for interesting processes. After that, an offline reconstruction of the data is performed and tighter selection criteria are applied to improve the signal to background ratio. A good background rejection is important to study the rare WS signal events.

In order to select D^* s, it is important to consider where they are different from background:

- Their decay products have a higher average momentum than particles which do not come from a decay of a heavy particle.
- The D^0 lifetime leads to a decay vertex which is mostly separated from the primary vertex. This can be exploited with selection criteria for the decay topology.

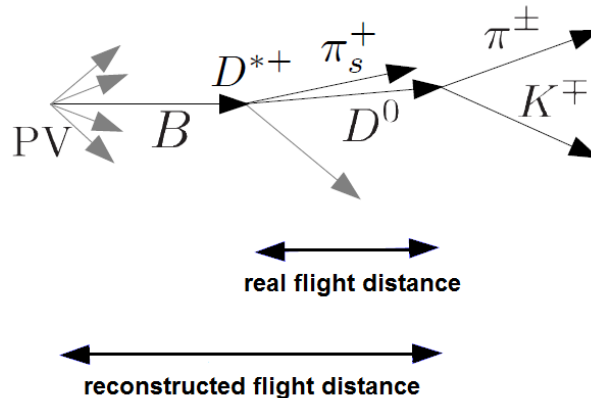


Figure 4.2: Sketch of non-prompt D^0 . PV denotes the primary vertex, grey arrows indicate additional particles in the event. The decay time is proportional to the flight distance. Therefore, a wrong reconstructed flight distance leads to a wrong lifetime.

- The quality of the reconstructed tracks of the D^0 decay products and their identification as pions and kaons can be used to reject background.

A summary of all selection criteria can be found in tables 4.1 and 4.2. They are discussed in the following sections.

4.4.1 Trigger

The first step of the data selection and reduction is the level 0 (L0) hardware trigger, based on VELO, calorimeter and muon system information. Particles (hadrons, muons, muon-pairs, electrons and photons) of high transverse momentum are reconstructed and selected based on particle type dependent thresholds¹. The threshold settings changed during the data taking periods. In addition, a multiplicity signal provided by the Scintillating Pad Detector is used to suppress events with several proton-proton interactions, which lead to a very high track multiplicity and complicate event reconstruction. The L0 trigger enhances the fraction of events with charm and b-hadrons and reduces the event rate to ≈ 1 MHz.

The high level trigger (HLT) is implemented in software. The first stage (HLT1) confirms the decision of the L0 trigger, performs a partial event reconstruction and adds the vertex information. In particular, events with displaced vertices are selected using the VELO information. The selection is optimized for events with decays of B mesons. D mesons are selected as well, as they have

¹In the L0, the particle type is associated with the subdetectors where the particle was detected.

similar characteristics. In 2010, the efficiency to select prompt D mesons was 10%. The HLT1 reduces the event rate to ≈ 30 kHz.

The second stage (HLT2) performs a full event reconstruction. Based on that, individual trigger lines can select events suitable for specific analyses. For the determination of the WS to RS ratio, two trigger lines which both select $D^{*+} \rightarrow D^0(\rightarrow K^\pm\pi^\mp)\pi_s^+$ are used. One line triggers on all events near the D^0 mass peak ("signal trigger"). The other one accepts a broader mass range ("widemass trigger"), but it is applied only to 10% of the events in order to reduce the data rate.

Due to trigger settings during the data-taking period of 2010, the D^0 mass sidebands around the signal peak are removed already at trigger level. This requires a different method to extract signal yields, as described in section 7.1.

The final selection of $D^{*+} \rightarrow D^0(\rightarrow K\pi)\pi_s^+$ uses several variables to further increase the signal significance. Based on a Monte Carlo study, the selection criteria were optimized to maximize the WS signal significance, $Sig_{WS} = \frac{N_{WS}}{\sqrt{N_{WS}+N_{BG}}}$, where N_{WS} is the number of selected WS events and N_{BG} is the number of background events under the signal peak [24].

4.4.2 Track momenta

Particles in background events have a smaller average momentum p and transverse momentum p_t than the signal events, therefore selection criteria on these variables are applied as shown in table 4.1.

Parameter	required value (MeV)
$p(\pi)$	>5000
$p_t(\pi)$	>900
$p(K)$	>5000
$p_t(K)$	>900
$p(\pi_s)$	>1600
$p_t(\pi_s)$	>260
$p_t(D^0)$	>3300
$p_t(D^*)$	>3600

Table 4.1: Selection criteria for momenta p and transverse momenta p_t of the particles.

4.4.3 Track and vertex fit quality

To remove tracks which are artefacts from the reconstruction program and do not correspond to real particles, a minimal quality of the track fit is required. All particles have to be detected in the VELO, the TT and the OT or IT subdetectors, therefore only tracks which pass all these detectors are regarded. Tracks with a

track fit quality of $\chi^2/ndf > 5$ are omitted in the analysis, where ndf is the number of degrees of freedom in the track fit. To calculate χ^2 , the difference between each measured parameter and the fit result is divided by the uncertainty of the measurement. The sum of the squares of these deviations is χ^2 . For real particles and a theoretical perfect detector description, the average χ^2/ndf is 1.

Similar to individual tracks, χ^2/ndf can be calculated for the combination of two or more particles to a common mother particle. For the combination of kaon and pion to a common vertex of the D^0 decay, $\chi^2/ndf < 5$ is required. For the decay vertex of the D^{*+} , a vertex quality of $\chi^2/ndf < 13$ is necessary.

4.4.4 Particle identification

The RICH subdetectors (see section 3.2.3) allow a separation of pions and kaons. For each particle, a likelihood of being a pion or a kaon (or another charged particle) is calculated. Mainly the misidentification of pions as kaons and vice versa is important in the analysis. Therefore, the difference of the logarithms of the likelihood to be a kaon and to be a pion is calculated. This value is called $DLL_{K-\pi}$. If it is positive the particle is more likely to be a kaon, if it is negative it is more likely to be a pion. The magnitude of the value corresponds to the quality of the distinction. A detailed description of the particle identification at LHCb can be found in [25].

A good particle identification is crucial for the analysis, as shown in section 5.3, therefore strong selection criteria are applied to $DLL_{K-\pi}$. For the kaon, $DLL_{K-\pi}(K) > 8$ is required, whereas the pion has to have $DLL_{K-\pi}(\pi) < -5$. For the π_s , the particle identification is not so crucial, therefore a looser selection of $DLL_{K-\pi}(\pi_s) < 3$ is sufficient.

4.4.5 Impact parameter

The impact parameter is the distance of closest approach of a track to the primary vertex. Therefore, particles from the primary vertex have a small measured impact parameter, whereas the D^0 daughters tend to have a larger impact parameter due to the D^0 flight distance. This allows a significant reduction of the combinatorial background, as most particles come from the primary vertex.

The error of the measured impact parameter depends on the transverse momentum of the particles. Instead of a selection based on the impact parameter, its significance is used, which is the measured impact parameter divided by the uncertainty of the measurement. This provides a better separation between tracks from D^0 and tracks from the primary vertex. A minimal separation significance of 3 standard deviations is required for both D^0 daughters.

The π_s should come from the primary vertex, therefore pions with an impact parameter larger than 0.08 mm are rejected.

4.4.6 Flight distance

To avoid having too many particles near the D^0 decay vertex, the significance of its flight distance from the primary vertex to the decay vertex has to be at least 4 standard deviations, and the absolute distance has to be at least 0.9 mm.

4.4.7 D^0 topology

The D^0 flight direction can be calculated from the momenta of its daughters K and π . This is compared to the direction given by the line between primary vertex and the D^0 decay vertex. The cosine of the angle α between both directions, $DIRA = \cos(\alpha)$ is calculated. Figure 4.3 shows the definition of α . For signal events, $DIRA$ is close to 1, a selection on $DIRA > 0.99995$ is applied to remove combinatorial background.

The point of closest approach to the primary vertex is calculated for both D^0 daughters. The angle between the pointing vectors from the primary vertex to these points, ξ is calculated. Figure 4.3 shows the definition of ξ . In the D^0 rest frame, kaon and pion fly away back to back. In the detector frame, this translates to a large ξ value. Only D^0 with $\cos(\xi) < -0.8$ are used for the analysis.

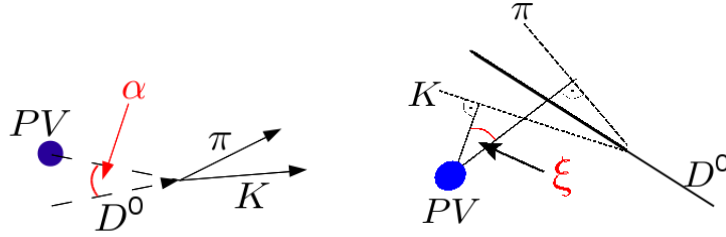


Figure 4.3: Sketch of the definitions of α (left) and ξ (right). The sketches are projections to two dimensions. In three dimensions, ξ can be different from the angle between K and π .

Particle	Parameter	required value
π	track χ^2/ndf	≤ 5
	$DLL_{K-\pi}$	≤ -5
	IP significance	$\geq 3\sigma$
K	track χ^2/ndf	≤ 5
	$DLL_{K-\pi}$	≥ 8
	IP significance	$\geq 3\sigma$
π_s	track χ^2/ndf	≤ 5
	$DLL_{K-\pi}$	≤ 3
	IP	$\leq 80\mu m$
D^0	vertex χ^2/ndf	≤ 5
	flight significance	$\geq 4\sigma$
	flight distance	$\geq 0.9mm$
	DIRA	≥ 0.99995
	$\cos(\xi)$	≤ -0.8
D^{*+}	vertex χ^2/ndf	≤ 13

Table 4.2: Summary of selection criteria, in addition to the criteria in table 4.1

Measurement method

5.1 Extraction of mixing parameters

In order to measure mixing parameters, the time-dependence of WS and RS decays has to be studied, as discussed in chapter 2. There are two methods to do this:

- A fit of the D^0 decay-time dependent rate of WS and RS decays. The mixing parameters R_{DCS} , x' and y' are a direct result of the fit. This requires a good knowledge of the decay time acceptance function, as the distributions of signal events are the product of the physical rate and the acceptance. This method was applied by BaBar [3] and Belle [2].
- A determination of the ratio of WS to RS decays in bins of the D^0 decay time. For each bin, the D^0 mass and δm distributions are fitted to extract the signal yield of WS and RS events, and the ratio $\frac{N_{WS}}{N_{RS}}$ is calculated. This results in a parabola described by the mixing parameters, as shown in chapter 2 and figure 8.1. A fit to the time-dependent ratio leads to R_{DCS} , x' and y' .

The binned method was used by CDF [1] and is used initially at LHCb, too. Compared to electron-positron colliders, hadron colliders like the Tevatron and the LHC have more background particles from the primary vertex which can lead to more combinatorial background. In order to suppress this background, selection criteria on variables like the impact parameter of the D^0 daughters or the separation of the D^0 decay vertex from the primary vertex have to be applied in the analyses. These selection criteria influence the D^0 decay time acceptance: D^0 with a long decay time are more likely to pass the selection than D^0 with a short decay time. In the binned method, acceptance effects cancel in first order, which makes this approach more favourable. As the physical ratio of WS to RS decays varies within bins, a decay time acceptance which varies within the bins can lead to effects of higher order, but this can be neglected.

5.2 Signal yield determination

To determine signal yields for RS and WS decays, a two-dimensional maximum likelihood fit within the RooFit toolkit [26] is used, where the D^0 mass m_{D^0} and δm are the input parameters. The distribution of the signal candidates is shown in figure 4.1. For each signal candidate, the likelihood \mathcal{P} of its $(m_{D^0}, \delta m)$ -values is given by the value of the fit function at this position, which depends on m_{D^0} , δm and additional parameters λ_l . The product of the likelihoods of all candidates then gives a measurement of the quality of the fit function. The fit method tries to maximize that product. To ease calculations, the negative logarithm of the likelihood is used. It can be written as:

$$-\ln \mathcal{L} = \sum_{i=1}^N \ln \mathcal{P}(m_{D^0}^i, \delta m^i, \lambda_l) \quad (5.1)$$

where the index i runs over the number of signal candidates and $m_{D^0}^i$, δm^i are the D^0 mass and δm of candidate i .

The default fit function includes the signal, the random slow pion background, the misreconstructed and the combinatorial background, as described in section 4.3. In total, 25 independent parameters are used to describe the signal and background shapes.

$$\begin{aligned} \mathcal{P}(m_{D^0}, \delta m) = & \mathcal{P}_{signal}(m_{D^0}, \delta m) \\ & + \mathcal{P}_{slowpi}(m_{D^0}, \delta m) \\ & + \mathcal{P}_{misrec}(m_{D^0}, \delta m) \\ & + \mathcal{P}_{combinatorial}(m_{D^0}, \delta m) \end{aligned} \quad (5.2)$$

For each component, the D^0 mass and δm are treated as independent, thus every component can be written as product of two one-dimensional distributions:

$$\begin{aligned} \mathcal{P}_{signal}(m_{D^0}, \delta m) &= N_{signal} \cdot \mathcal{P}_{signal}^{m_{D^0}}(m_{D^0}) \cdot \mathcal{P}_{signal}^{\delta m}(\delta m) \\ \mathcal{P}_{slowpi}(m_{D^0}, \delta m) &= N_{slowpi} \cdot \mathcal{P}_{slowpi}^{m_{D^0}}(m_{D^0}) \cdot \mathcal{P}_{slowpi}^{\delta m}(\delta m) \\ \mathcal{P}_{misrec}(m_{D^0}, \delta m) &= N_{misrec} \cdot \mathcal{P}_{misrec}^{m_{D^0}}(m_{D^0}) \cdot \mathcal{P}_{misrec}^{\delta m}(\delta m) \\ \mathcal{P}_{combinatorial}(m_{D^0}, \delta m) &= N_{combinatorial} \cdot \mathcal{P}_{combinatorial}^{m_{D^0}}(m_{D^0}) \cdot \mathcal{P}_{combinatorial}^{\delta m}(\delta m) \end{aligned} \quad (5.3)$$

All individual shapes get normalized to have an integral of 1 over the signal region, therefore $N_{component}$ is the number of events corresponding to this component.

5.2.1 Signal shape

The signal shape uses gaussian distributions f_G and Crystal Ball functions f_{CB} [27]. The Crystal Ball function f_{CB} is given by

$$f_{CB}(x, \bar{x}, \sigma, \alpha, n) = N \cdot \begin{cases} \exp\left(-\frac{(x-\bar{x})^2}{2\sigma^2}\right) & \text{for } \frac{x-\bar{x}}{\sigma} > -\alpha \\ A \cdot \left(B - \frac{x-\bar{x}}{\sigma}\right)^{-n} & \text{for } \frac{x-\bar{x}}{\sigma} \leq -\alpha \end{cases} \quad (5.4)$$

with $A = \left(\frac{n}{\alpha}\right)^n \cdot \exp\left(-\frac{|\alpha|^2}{2}\right)$ and $B = \frac{n}{|\alpha|} - |\alpha|$ and a normalization factor N . x is the measured physical parameter, which is either m_{D^0} or δm . The Crystal Ball function is similar to a gaussian distribution with mean value \bar{x} and standard deviation σ , but has a larger tail towards one side which is described by the parameters α (region of the tail) and n (shape of the tail).

The δm distribution of the signal is modelled as the sum of two gaussian distributions f_G and a Crystal Ball function f_{CB} , where the gaussians share the same mean value.

$$\mathcal{P}_{signal}^{\delta m}(\delta m) = p_1 \left[p_2 f_G(\delta m, \overline{\delta m}_1, \sigma_{\delta m,1}) + (1 - p_2) f_G(\delta m, \overline{\delta m}_1, \sigma_{\delta m,2}) \right] + (1 - p_1) f_{CB}(\delta m, \overline{\delta m}_2, \sigma_{\delta m,3}, \alpha_{\delta m}, n_{\delta m}) \quad (5.5)$$

where p_1 and p_2 describe the relative size of the gaussians and the Crystal Ball function. $\overline{\delta m}_1$ and $\overline{\delta m}_2$ are the mean values of the gaussian distributions and the Crystal Ball function, respectively. $\sigma_{\delta m,1}$, $\sigma_{\delta m,2}$ and $\sigma_{\delta m,3}$ are parameters for the widths of the individual parts.

The Crystal Ball function for the signal has a slightly higher mean value and a tail to higher δm values, which is described with the parameters α and n . In radiative events, one or more additional photons are generated: In these events, the D^0 momentum measurement is wrong, which leads to an incorrect calculation of δm from the combination of D^0 and π_s to a D^{*+} . In most cases, the δm is increased in this process, leading to entries with higher δm in the signal shape. The Crystal Ball function is used to describe these entries.

The D^0 mass distribution of the signal consists of a gaussian distribution and a Crystal Ball function with the same mean value. The tail of the Crystal Ball function reaches towards the low D^0 mass region and again accounts for radiative events, where the reconstructed mass is too low due to the photons which are not reconstructed.

$$\mathcal{P}_{signal}^{m_{D^0}}(m_{D^0}) = p_3 f_G(m, \overline{m}_1, \sigma_{m,1}) + (1 - p_3) f_{CB}(m, \overline{m}_1, \sigma_{m,2}, \alpha_m, n_m) \quad (5.6)$$

5.2.2 Random slow pion background shape

As δm distribution of the random slow pion background, a special function which was developed by BaBar [3] is used. It is implemented in the RooFit toolkit as *RooDstD0BG*.

$$\mathcal{P}_{slowpi}^{\delta m}(\delta m) = f_{DstD0BG}(\delta m) = \left(\frac{\delta m}{A}\right)^2 \left(1 - e^{-\frac{\delta m - D}{C}}\right) + B \left(\frac{\delta m}{D} - 1\right) \quad (5.7)$$

D is the δm value where the function is equal to zero, C determines the curvature for low δm values, and A and B define the shape for higher δm values.

The D^0 mass distribution is shared with the signal, as it is the distribution of correctly reconstructed D^0 particles.

$$\mathcal{P}_{slowpi}^{m_{D^0}}(m_{D^0}) = \mathcal{P}_{signal}^{m_{D^0}}(m_{D^0}) \quad (5.8)$$

5.2.3 Combinatorial background shape

Purely combinatorial background is modelled with a linear distribution in the D^0 mass, r_1 and r_0 are free parameters.

$$\mathcal{P}_{combinatorial}^{m_{D^0}}(m_{D^0}) = r_1 \cdot m_{D^0} + r_0 \quad (5.9)$$

The δm distribution is shared with the random slow pion background, as both come from pions which are not associated to a D^0 .

$$\mathcal{P}_{combinatorial}^{\delta m}(\delta m) = \mathcal{P}_{slowpi}^{\delta m}(\delta m) \quad (5.10)$$

5.2.4 Misreconstructed background shape

For the D^0 mass distribution of misreconstructed background, a polynomial of second order is used. It has 3 free parameters s_0 , s_1 and s_2 .

$$\mathcal{P}_{combinatorial}^{m_{D^0}} = s_2 \cdot (m_{D^0})^2 + s_1 \cdot m_{D^0} + s_0 \quad (5.11)$$

The δm distribution is described with a single gaussian, as the fit is not sensitive to more detailed structures with the current sample size.

$$\mathcal{P}_{combinatorial}^{\delta m}(\delta m) = f_G(\delta m, \overline{\delta m}_{misrec}, \sigma_{\delta m, misrec}) \quad (5.12)$$

5.2.5 Fitting method

All parameters describing the shape of the distributions are determined with events triggered by the widemass trigger (see section 4.4.1). Here, the fit is more sensitive to the D^0 mass sidebands. These parameters are fixed and used in a fit to all signal events.

To improve the determination of the WS signal, the parameters of the shape of the signal contribution are fixed to the values obtained from the fit to RS events. One-dimensional projections of the two-dimensional fit are shown in figure 5.1. A good agreement between data and fit function is observed, and the signal and background components can be separated within the fit.

5.2.6 Alternative method

CDF [1] determined the signal yield without performing a two-dimensional fit. In order to do this, the m_{D^0} , δm plane is divided into several bins of δm . In each bin, the yield of the D^0 mass peak is determined with a one-dimensional fit to the D^0 mass distribution. This number contains the events of the signal and the random slow pion background, the combinatorial and misreconstructed background do not peak in the D^0 mass and therefore do not contribute to the yields. These values of the yields are then used to get a one-dimensional, binned distribution in δm , and the signal yield is determined from this distribution with an additional fit which separates signal and random slow pion background.

While it is easier to perform the individual fits, it adds an extra step in the analysis which is not necessary if a two-dimensional fit is possible.

5.3 Double misidentified events

In the detector, kaons can be misidentified as pions and vice versa. If that happens for both particles at the same time, $D^0 \rightarrow K^- \pi^+$ (RS decay) can be misidentified as $D^0 \rightarrow K^+ \pi^-$ (WS decay). This leads to an increased number of WS events and modifies the ratio of WS to RS events.

The misidentification of a WS decay $D^0 \rightarrow K^+ \pi^-$ as RS decay $D^0 \rightarrow K^- \pi^+$ is also possible, but negligible as the expected WS signal is smaller by a factor of ≈ 250 .

As an example: a double misidentification probability as small as $P_{misid} = 0.1\%$ would give additional events reconstructed as WS which have 0.1% the size of the RS signal - that is $\frac{1}{4}$ of the expected WS signal and much larger than the statistical uncertainty of the WS analysis.

Two methods are presented to handle the influence of these events on the WS to RS ratio.

5.3.1 Mass exchange method

A D^0 with a correct identification of the daughter particles has a reconstructed mass distribution which peaks at the true D^0 mass and has a width (corresponding to 1 standard deviation) of ≈ 8 MeV. With a wrong particle assumption, the relativistic 4-momenta of the particles are wrong, and the calculated D^0 mass is much broader, as shown in figure 5.2.

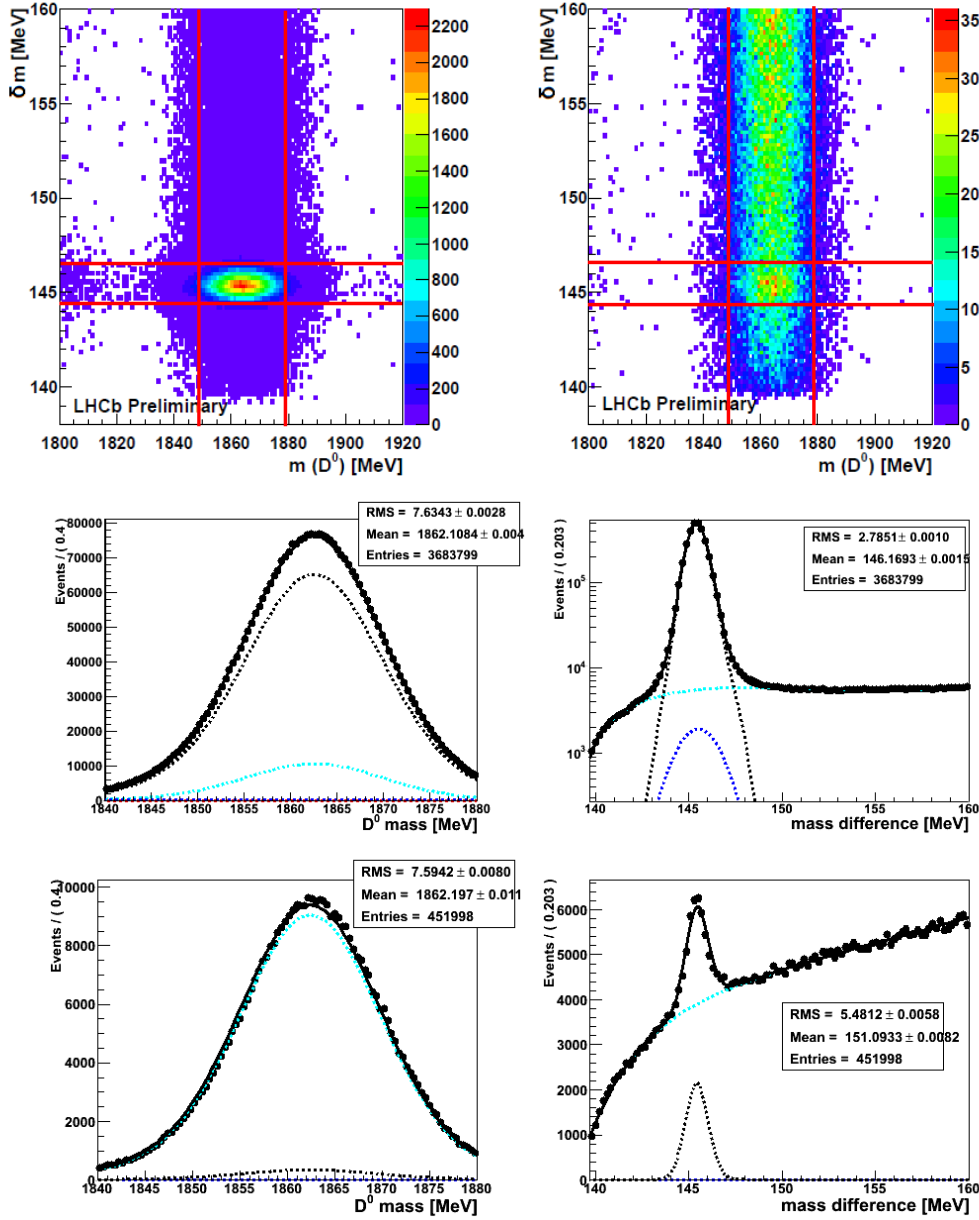


Figure 5.1: Two-dimensional distribution of RS (upper left figure) and WS (upper right figure) events, the lines show the signal box and sideband regions. Projections of the two-dimensional fits of RS (middle figures) and WS (lower figures) events to the D^0 mass (left) and δm (right). Signal is black, random slow pion background is cyan and misreconstructed background is blue. The combinatorial background in red is too small to be visible within the figures. The δm projection of RS events is shown with a logarithmic scale.

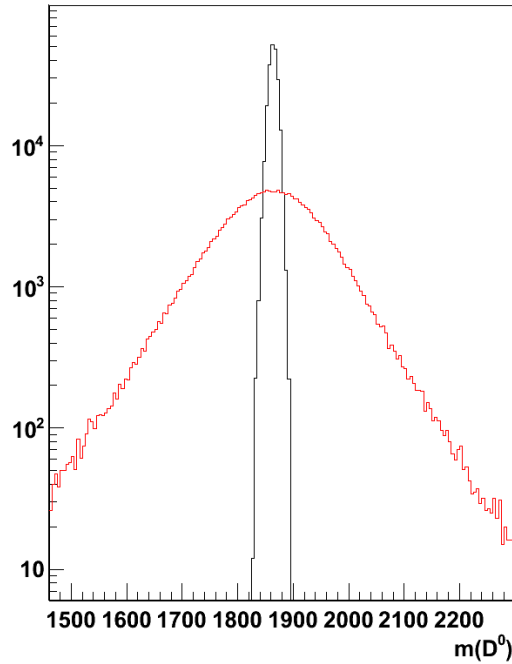


Figure 5.2: m_{D^0} distribution of RS signal events (black) and of the same events but with swapped masses for kaons and pions (red). The broad red distribution corresponds to events where both particles were misidentified. The fraction of events which is between $1836.5 \text{ MeV} < m_{D^0} < 1892.7$ corresponds to P_{right} (black distribution) and P_{wrong} (red distribution), as defined in section 5.3.1.

This can be exploited to reject D^0 mesons which are misidentified. The 4-momenta of the daughters are recalculated with the opposite particle hypothesis: The pion is treated as kaon with the kaon mass and for the kaon, the pion mass is used. Both particle momenta are then combined to a fake D^0 and its invariant mass is calculated.

If the original D^0 had a misidentification of both daughters, the new mass calculation uses correct daughter masses and is likely to be near the D^0 mass. Events in the D^0 mass region of $1836.5 \text{ MeV} < m_{D^0} < 1892.7 \text{ MeV}$ with the new calculation can be rejected. The mass region is chosen around the signal peak in a way that $P_{\text{right}} = 98\%$ of the correctly identified particles lie within this region. That means that the selection rejects 98% of the double misidentification background, as the new mass calculation yields the mass with the right particle identification there.

Even for correct D^0 daughter identifications, by chance the result of the new

mass calculation can lie in the same region. This can happen when kaon and pion have a similar absolute momentum. In that case, the swap of the mass hypotheses leads to a very similar calculated mass and the events are more likely to be removed. This can be seen in figure 5.3 showing the logarithm of the momentum ratio $\log(P_\pi/P_K)$: The dip around 0 corresponds to D^0 decays with a similar absolute momentum of both daughters. About $P_{wrong} = 23\%$ of the signal with correct particle identification is lost for the analysis with this selection.

Using these numbers, it is possible to evaluate the probability of a double misidentification on data, as shown in appendix A.1. In the dataset of 2010, no significant number of double misidentified events could be found.

The mass exchange method was applied on 2010 data, as it provides a way to remove double misidentified events without access to the D^0 mass sidebands. In the dataset of 2011, these mass sidebands can be used in a fit to the data as described below. Therefore, it is not necessary to apply the mass exchange method there.

5.3.2 Misidentified events included in fit

The broad mass distribution of the misidentified D^0 as shown in figure 5.2 allows to treat them as background contribution, similar to misreconstructed background. The distribution of both misreconstructed and misidentified background together can be described with a parabolic shape for the D^0 mass. This shape is included in the fit to data and background, therefore misidentified D^0 are not counted as signal events.

Due to the removal of the D^0 mass sidebands in the trigger (see section 4.4.1), this is not possible with the dataset of 2010. The dataset of 2011 allows to perform a full two-dimensional fit including sidebands, therefore the misidentified background can be included there.

5.4 Asymmetries

Several asymmetries can be present in the analysis. While they cancel in the WS to RS ratio in first order, it is nevertheless important to study them as the presence of several asymmetries at the same time can lead to higher order effects which influence the measured WS to RS ratio.

5.4.1 Production asymmetry

The initial collision of two protons is not symmetric under charge conjugation and contains six valence quarks. This can lead to asymmetric production rates of particles and antiparticles. This changes the ratio between D^{*+} and D^{*-} but does not change the WS/RS ratio of D^{*+} and D^{*-} decays. Here, it is assumed

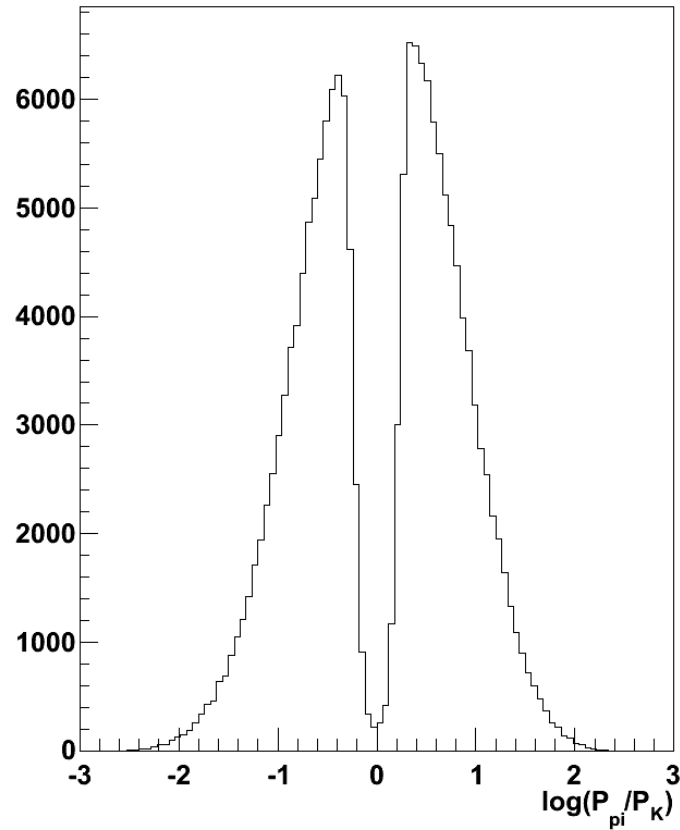


Figure 5.3: *Distribution of $\log(P_\pi/P_K)$ after the mass exchange selection is applied. The logarithm of the ratio is chosen to show the symmetry of the system. The dip around 0 comes from the mass exchange method and corresponds to events where kaon and pion have a similar absolute momentum. The slightly asymmetric shape comes from the difference between kaon and pion mass, which leads to a small difference in the momentum distribution.*

that CP violation is negligible, so the WS/RS ratio is the same for D^{*+} and D^{*-} . Therefore, this asymmetry alone does not give any bias. This can be concluded from the calculation in section 5.4.3 in the case of no detection asymmetry.

5.4.2 Slow pion detection asymmetry

The detector response to particles and antiparticles is not exactly the same. This can lead to different probabilities to detect π_s^+ and π_s^- . The result is similar to a production asymmetry, as it changes the ratio of selected D^0 to \overline{D}^0 candidates

at production time. In addition, the magnetic field can modify the detection asymmetry, as described in section 5.4.4.

5.4.3 D^0 daughter detection asymmetry

Similar to the π_s asymmetry, the detector can have a different probability to detect $K^-\pi^+$ versus $K^+\pi^-$. Both decay products appear in both WS and RS events, so the naive expectation would be that they cancel as well. However, this is wrong, if it is combined with the production and π_s detection asymmetry:

Let N_{D^0} be the number of produced D^{*+} decays where the π_s^+ is detected and let $\epsilon_{K^-\pi^+}$ be the detection efficiency of the (RS) D^0 decay. Similarly, $N_{\overline{D}^0}$ and $\epsilon_{K^+\pi^-}$ are defined. The time-dependence is not considered here, therefore the ratio of WS to RS decays is fixed and defined as R . In addition, CP violation is neglected, this leads to a single value of R for both D^0 and \overline{D}^0 , as shown in chapter 2.

Now, the number of detected and selected WS events is

$$N_{WS} = \epsilon_{K^+\pi^-} N_{D^0} R + \epsilon_{K^-\pi^+} N_{\overline{D}^0} R \quad (5.13)$$

and the number of RS events is

$$N_{RS} = \epsilon_{K^-\pi^+} N_{D^0} + \epsilon_{K^+\pi^-} N_{\overline{D}^0} \quad (5.14)$$

The ratio of both can be simplified by defining $A_{prod} = \frac{N_{D^0}}{N_{\overline{D}^0}}$ and $f_{det} = \frac{\epsilon_{K^-\pi^+}}{\epsilon_{K^+\pi^-}}$, which leads to

$$\frac{N_{WS}}{N_{RS}} = R \frac{A_{prod} + f_{det}}{1 + A_{prod} \cdot f_{det}} \quad (5.15)$$

In the presence of a $K\pi$ detection asymmetry $f_{det} \neq 1$ and a production asymmetry $A_{prod} \neq 1$ at the same time, the ratio of WS to RS decays is not equal to R . That means that the asymmetries can change the measured ratio of WS to RS decays.

In principle, it is possible to determine and to remove these asymmetries on data. This is described in appendix A.2.

5.4.4 Magnet polarity and spatial asymmetry

The magnetic field (see section 3.2.2) bends particles of opposite charge to different sides of the detector. A spatial asymmetry of the detector can lead to asymmetric detection probabilities for particles. This is in particular important for π_s , as they have a low average momentum and therefore a large bending angle in the magnet. The bending angle leads to regions in the D^{*+} and D^0 phase space where only π_s^+ or only π_s^- can be detected, which is similar to a production asymmetry of 100%. In the p, p_x plane of the π_s , where p_x is the momentum in x-direction, these regions lead to the edges visible in figure 5.4. π_s^+ with positive

p_x and low p with negative magnet polarity are likely to leave the detector acceptance, therefore the edges in the upper left figure are shifted towards negative p_x . The same is true for π_s^- with positive magnet polarity. For π_s^+ with positive magnet polarity and π_s^- with negative magnet polarity, the situation is reversed and the momentum distribution is shifted towards positive p_x . To evaluate the influence of this detection asymmetry, the regions where only one π_s charge can be detected can be excluded from the analysis. A shift in the observed ratio of WS to RS events is a measure of the size of this effect.

In order to suppress effects from the magnet, its polarity is switched several times during the data taking periods. As a cross-check, the analysis can be done with both magnet polarities separated.

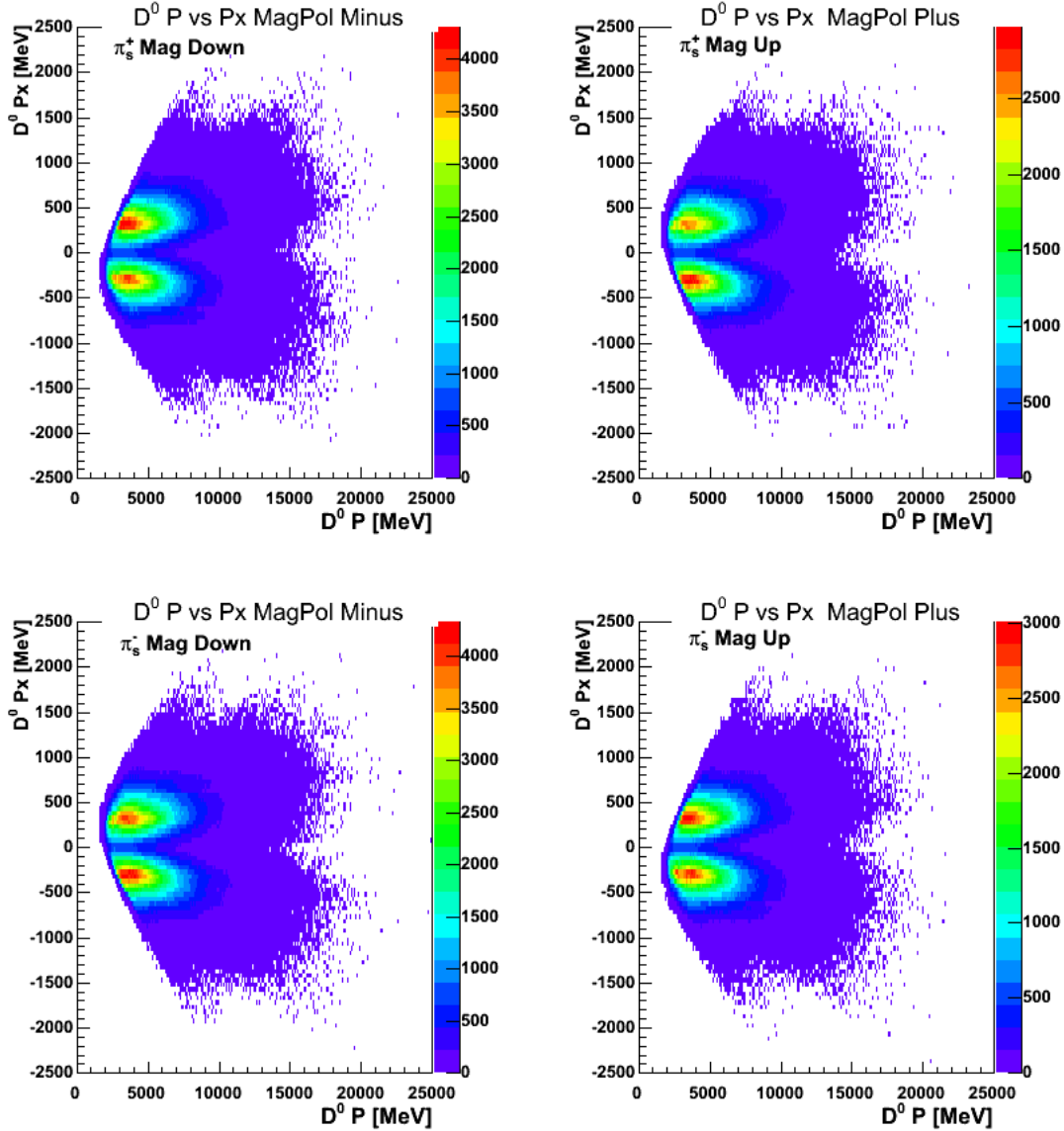


Figure 5.4: Distributions of the momentum P (x-axis) and momentum in x-direction P_x (y-axis) of the π_s . The upper left figure shows positive π_s^+ with negative magnet polarity. This means that π_s^+ are bent towards positive p_x in the magnet. Low-energetic pions with a high positive p_x are bent out of the geometric acceptance of the LHCb detector and cannot be measured. With a reversed magnet polarity (upper right), the same happens for negative p_x . The lower figures show the distributions for π_s^- . Due to their opposite charge, the role of the magnetic field is reversed here. Therefore, π_s^+ with negative magnet polarity (upper left) show the same distribution as π_s^- with positive magnet polarity (lower right), and π_s^+ with positive magnet polarity (upper right) are similar to π_s^- with negative magnet polarity (lower left). The lower probability to find pions of any momentum at $p_x \approx 0$ comes from the requirement of a minimal transverse momentum.

Background from non-prompt D^0

6.1 Introduction

The energy which is released in the $D^{*+} \rightarrow D^0\pi$ decay, $m(D^*) - m(D^0) - m(\pi)$, is small compared to the particle masses. Therefore, the decay products of the D^{*+} , π_s and D^0 have a small angle between their flight directions. This leads to large errors in the reconstruction of the D^{*+} decay vertex.

As the D^{*+} decays via the strong interaction, its lifetime is extremely short and the primary proton-proton interaction vertex (PV) approximates with high precision the D^{*+} decay vertex. The D^0 mixing analysis assumes that all D^{*+} originate from the PV. D^{*+} and D^0 from the PV are called prompt D^{*+} and D^0 . Alternatively, the D^{*+} decay vertex can be reconstructed from its daughter particles.

The downside of using the PV is that the D^0 gets a wrong decay time assignment if the D^{*+} does not come from the PV, but is itself a decay product of an unstable particle as it happens for example for B-mesons (non-prompt D^{*+} and D^0). Depending on the selection criteria, about 5-8% of the D^0 sample consists of non-prompt D^0 s from B-meson decays.

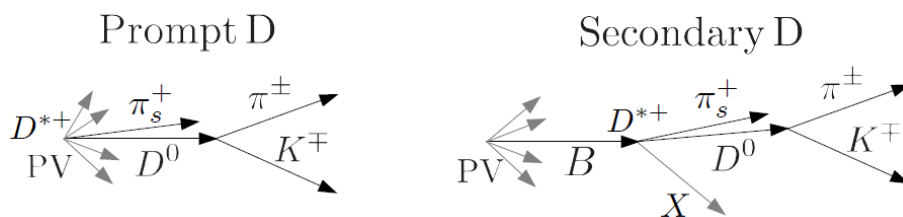


Figure 6.1: Sketch of the particle decays for prompt (left) and non-prompt (right) D^0 . PV denotes the primary vertex.

For the mixing measurement the time-dependence of WS to RS decays is determined. The wrong decay time measurement for non-prompt D^0 leads to

a shift of the measured mixing parameters. A typical lifetime of a B-meson is 1.5 ps , while the lifetime of a D^0 is only 0.41 ps . That means that non-prompt D^0 via the decay chain $B \rightarrow D^*(\rightarrow D^0\pi_s)X$ get a larger decay time assigned than prompt D^0 .

Without acceptance and selection effects, it is possible to compare the time-evolution of prompt and non-prompt D^0 analytically. The distribution of prompt D^0 is given by an exponential with the decay constant $\Gamma_D = 1/\tau_D$:

$$\frac{dN_p(t)}{dt} \propto \Gamma_D \cdot e^{-\Gamma_D t} \quad (6.1)$$

For non-prompt D^0 , the probability for a decay at time t can be expressed with an integration over the decay time t' of the B meson with an average decay constant $\Gamma_B = 1/\tau_B$. The differences in the lifetimes of the individual B-mesons are neglected here.

$$\frac{dN_s(t)}{dt} \propto \int_0^t dt' \Gamma_B e^{-\Gamma_B t'} \Gamma_D e^{-\Gamma_D(t-t')} \quad (6.2)$$

$$= \Gamma_B \Gamma_D e^{-\Gamma_D t} \int_0^t dt' e^{(\Gamma_D - \Gamma_B)t'} \quad (6.3)$$

$$= \frac{\Gamma_B \Gamma_D}{\Gamma_D - \Gamma_B} e^{-\Gamma_D t} (e^{(\Gamma_D - \Gamma_B)t} - 1) \quad (6.4)$$

$$= \frac{\Gamma_B \Gamma_D}{\Gamma_D - \Gamma_B} (e^{-\Gamma_B t} - e^{-\Gamma_D t}) \quad (6.5)$$

The total number of non-prompt D^0 is smaller than the number of prompt D^0 , but for $t \gg \tau_D$, its fraction increases due to the large B meson lifetime.

The data selection, mainly the DIRA (see section 4.4.7) and impact parameter (section 4.4.5) criteria, suppresses non-prompt D^0 from B-mesons with large decay time, but they are not sufficient to reduce the background to a negligible level. However, they are effective in reducing non-prompt D^0 which come from long-living B-mesons, therefore the error in the decay time measurement for remaining non-prompt D^0 is much smaller than the long B-meson lifetime and equation (6.5) suggest.

The time-dependent fit of the WS to RS ratio is very sensitive to the region of large decay times, which enhances the effect of non-prompt D^0 on the mixing parameters in this region. A mixing analysis needs a method to take contributions from non-prompt D^0 into account.

Two techniques to handle the non-prompt background are presented here.

6.2 Impact parameter fit

This method was used by CDF [1]. D^0 from the primary vertex have a small measured impact parameter, whereas D^0 from decays of B mesons can have a

larger impact parameter. This difference can be exploited in a fit to the impact parameter distribution, which allows to estimate the relative fractions of prompt and non-prompt D^0 . The fit has to be done in each bin of the D^0 decay time for a binned analysis or as a time-dependent function, both for WS and RS events. An example of an impact parameter distribution with fitted prompt and non-prompt contributions is shown in figure 6.2.

The shapes of prompt D^0 and non-prompt D^0 have to be estimated from Monte Carlo simulation studies, therefore a good agreement between Monte Carlo and data is required.

The advantage of this method is the direct access to the number of non-prompt D^0 both in WS and RS events, so they can be subtracted from data. However, for large decay times, the small amount of remaining simulated events leads to large statistical uncertainties in the impact parameter distributions, which can lead to large uncertainties with this method.

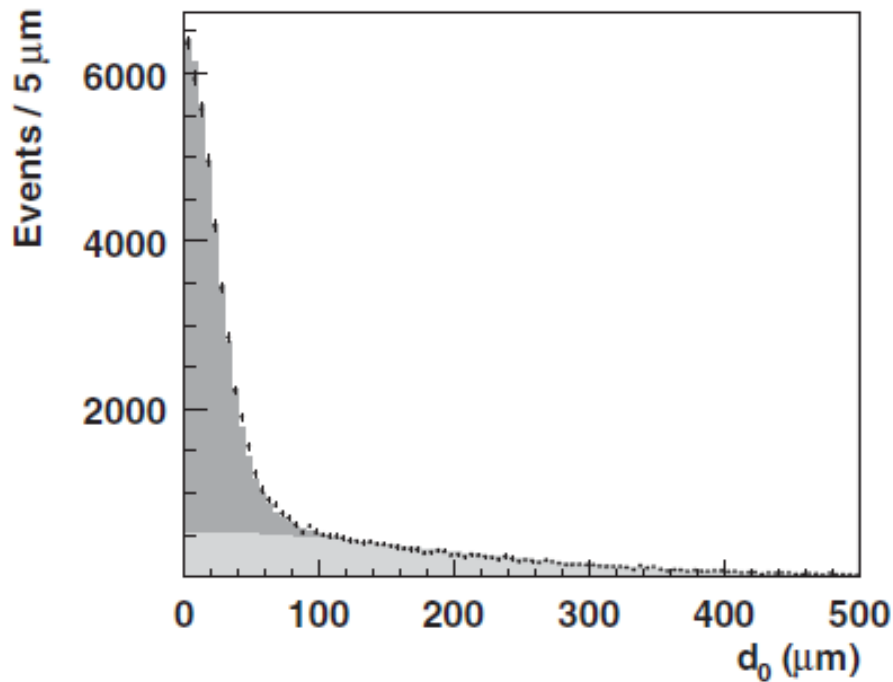


Figure 6.2: Impact parameter (d_0) distribution for prompt (dark grey) and non-prompt (light grey) D^0 , taken from the CDF publication on charm mixing [1].

6.3 Reconstruction of non-prompt D^0

In some events with a non-prompt D^{*+} , it is possible to reconstruct the B-hadron which produced the D^{*+} . From the B decay vertex the decay time of the non-prompt D^0 can be obtained. These events can be used to estimate the error on the reconstructed decay time and the influence on the measured mixing parameters caused by non-prompt D^0 , without using Monte Carlo simulations. This makes the analysis less dependent on a good agreement between data and Monte Carlo simulations.

In order to apply this method, a reconstruction and selection of the B-hadron decay has been developed in the context of this thesis, and its suitability has been tested in Monte Carlo and data studies. It is not possible to reconstruct all decays of B-hadrons. The composition of the different B-hadron decay channels has been studied, and a channel which allows the reconstruction of a representative sample of non-prompt D^0 is presented. In addition, the total fraction of non-prompt D^0 can be determined. This is possible with the distribution of the impact parameter of the D^0 , as prompt and non-prompt D^0 disentangle in this variable.

While the dataset of 2010 is too small to apply this method, the dataset of 2011 can be used to perform a reconstruction of non-prompt D^0 . RS and WS events have a different time-dependence for both prompt and non-prompt D^0 . The number of reconstructible non-prompt WS events is too small to analyse them, but the sample of RS events is sufficient to study the non-prompt D^0 events.

6.3.1 Suitable B hadron decay channels

To avoid an influence on the decay time distribution in the selection of non-prompt D^0 , the selection cannot restrict variables like the impact parameter of particles which are used in other analyses to reduce the background, especially to remove particles from the primary vertex. This means that the reconstructed decay channel must provide a way to reduce the background without these selection criteria. At the same time, it should provide a sample which is large enough to draw statistical significant conclusions.

The decay $\bar{B} \rightarrow D^{*+} \mu^- \nu(X)$, where (X) denotes possible additional particles, was found to be the best channel for these requirements. The high-energetic muons produced in the decay are easy to identify in the LHCb detector (see chapter 3), and the muon in semileptonic B decays suppresses combinatorial background.

6.3.2 Selection of $B \rightarrow D^* \mu \nu (X)$

For all D^{*+} which pass the regular D^{*+} selection and lie in the signal region ($1843 \text{ MeV} < m(D^0) < 1885 \text{ MeV}$ and $144.02 \text{ MeV} < \delta m < 146.84 \text{ MeV}$), a muon

is searched which is combined with the D^{*+} to form a secondary vertex of a B-meson decay. After that, most background candidates are removed via selection criteria.

The selection for the decay $\bar{B} \rightarrow D^{*+}\mu\nu(X)$ has to be inclusive, as the neutrino cannot be detected and additional particles may appear in the decay. This means that the reconstructed mass for the combination of the D^{*+} and the muon (pseudo B meson mass) lies between the sum of their masses and the B meson mass. The level of combinatorial background can be estimated from the mass region above the mass of B mesons. The left distribution in figure 6.3 shows the reconstructed pseudo B^0 mass (as combination of D^{*+} and muon), including the upper sideband. In addition, the selected events can be compared with the amount of "wrong sign" combinations of $D^{*+}\mu^+$, as these are very unlikely in a B decay.

In general, the selection applied here is loose - the D^{*+} selection already removes most of the non- D^{*+} background, and uncorrelated high-energetic muons are rare. For the D^{*+} selection and a description of the variables, see section 4.4. In addition, the following criteria are applied:

- D^{*+} flight significance: < 2
- Muon: $DLL(\mu - \pi) > 3$, $p_t > 3\text{GeV}$, $\chi^2/ndf(track) < 5$
- Reconstructed B meson: $m_B < 5.5\text{GeV}$, $\chi^2/ndf < 3$
- Reconstructible particles fly towards the detector (positive z-direction), therefore the z-positions of the vertices have to be in the correct order:
 $z_{PV} < z_{Bdecay} < z_{Ddecay}$

The distribution in the pseudo B^0 mass and $p_t(\mu)$ is shown in figure 6.3. Signal events are the horizontal band inside the signal box, background from random muons accounts for the vertical band. After the selection, about 40000 events are observed in the dataset taken in 2011.

Compared to the sample of all prompt D^0 , the non-prompt D^0 have larger decay times and different shapes in correlated variables like impact parameter, flight significance, DIRA and $\cos(\xi)$ (for an explanation of these parameters, see section 4.4). In all other variables, the prompt and non-prompt D^0 show a good agreement. This is shown in figures 6.4 and 6.5.

6.3.3 Comparison to simulation

To use the selected sample of non-prompt D^0 , it is necessary that it is representative for the total background from non-prompt D^0 . This requires that both samples agree in their distributions of impact parameters and D^0 decay time, as these variables are used to estimate the influence of non-prompt D^0 background on the mixing parameters, as discussed in section 6.3.4 and 6.3.6. Differences in the distributions lead to systematic uncertainties. A study was performed, based on three different datasets:

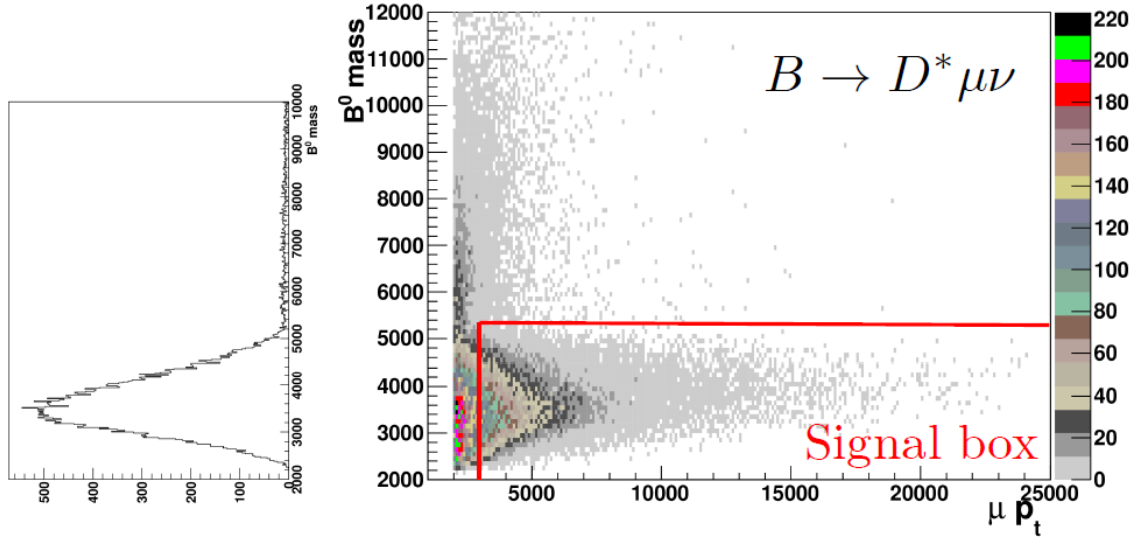


Figure 6.3: *Right: Two-dimensional distribution of the reconstructed pseudo B^0 mass and the transverse momentum $p_t(\mu)$ of the muon for selected non-prompt D^0 after all other selection criteria are applied. The box of the final selection is shown. Left: Projection to the pseudo B^0 mass after application of the $p_t(\mu)$ selection. The high mass region shows the low level of remaining combinatorial background.*

Parameter	required value
D^{*+} flight significance	≤ 2
μ $DLL_{\mu-\pi}$	≥ 3
μ p_t	$\geq 3 \text{ GeV}$
μ track χ^2/ndf	≤ 5
B meson mass	$\leq 5.5 \text{ GeV}$
B meson vertex fit χ^2/ndf	≤ 3
vertex ordering	$z_{PV} < z_{Bdecay} < z_{Ddecay}$

Table 6.1: *Summary of selection criteria for non-prompt D^0 . They are applied in addition to the D^{*+} selection, as described in section 4.4.*

- Simulated decays of $\overline{B^0} \rightarrow D^{*+} \mu^- \nu_\mu$ with the default selection of prompt D^0 . The decay channel $\overline{B^0} \rightarrow D^{*+} \tau^- (\rightarrow \mu^- \nu_\mu \nu_\tau) \nu_\tau$ was included in this sample, as it has a very similar structure ("Semileptonic sample").
- Simulated events of an inclusive B meson sample (i.e. B mesons of all types and all decay channels). The default selection of prompt D^0 is used ("inclusive B sample").

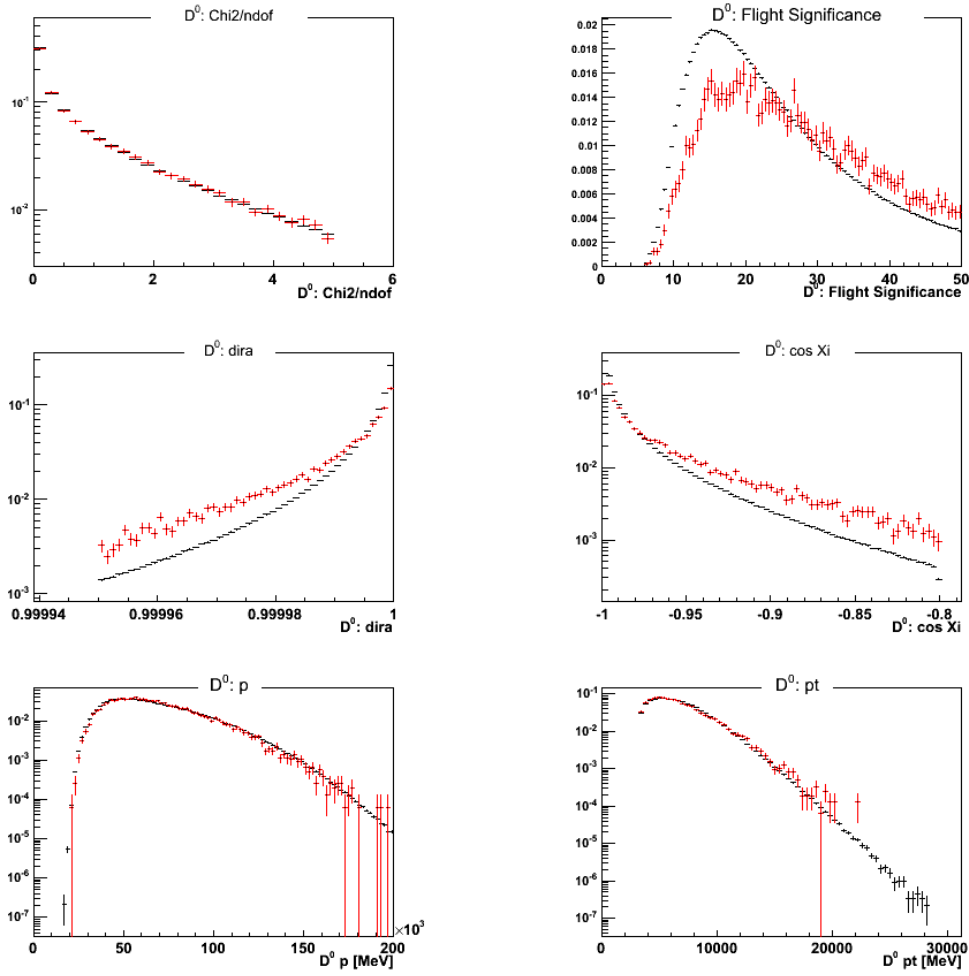


Figure 6.4: Comparisons between all selected D^0 (black) and the non-prompt D^0 subsample (red), normalized to 1. The upper row shows the quality of the D^0 vertex fit (left) and the D^0 flight significance (right), as measured from the primary vertex. The vertex fit quality is not affected by the non-prompt D^0 reconstruction, but the selected non-prompt D^0 have larger flight distances, as expected. The middle row shows the DIRA (left) and $\cos(\xi)$ (right) distribution. It can be seen that the selection in these two variables suppresses background from non-prompt D^0 , as it has a broader distribution than the prompt signal events. The lower row shows the momentum and transverse momentum of the D^0 . No significant difference is observed.

- Selected sample of non-prompt D^0 from data ("Data sample")

An analysis of the different B decay channels of the inclusive B sample shows that about 3% of the events in this sample consist of $\overline{B^0} \rightarrow D^* \mu \nu_\mu$. 54% are two-body decays, this includes decays to resonances or short-living particles which can decay into several other particles. 41% are three-body decays (including $\overline{B^0} \rightarrow D^* \mu \nu_\mu$), and 5% of the decays go to at least 4 particles. This means that at most 3% of the non-prompt background can be reconstructed, even if all muons would be detected and passed the selection.

Comparisons between different decay channels and between Monte Carlo simulations and data for the D^0 impact parameter and D^0 decay time (when reconstructed as prompt D^0) are shown in figures 6.6 to 6.9. In general, no large deviations are visible, which shows that the decay channel $\overline{B^0} \rightarrow D^{*+} \mu^- \nu_\mu$ is representative for the whole non-prompt background. In addition, it shows that the simulated events with B mesons have similar distributions to the reconstructed non-prompt D^0 on data. The existing differences between the two simulated samples can be used to estimate the systematic errors of the procedure.

The comparison between data and Monte Carlo is a crosscheck for the whole procedure. The compared samples have a different origin and selection:

- The first sample was taken from data with the selection of non-prompt D^0 applied as discussed above, where most D^0 are prompt and the selection has to find the non-prompt particles inside.
- The latter sample is extracted from a simulation of only non-prompt D^0 with the selection of prompt D^0 .

In spite of this different origin, both samples consist of the same event type: Non-prompt D^0 which are selected in the default (prompt) D^0 selection.

6.3.4 Application to data

Although the subsample of non-prompt D^0 obtained with the semileptonic reconstruction accounts only for $\approx 2\%$ of the total non-prompt background, the shape of the $\log(IP)$ and D^0 decay time distribution of these events agree well with all other non-prompt D^0 . The two-dimensional distributions of prompt and non-prompt D^0 in these variables are shown in figure 6.10.

To obtain the total amount of non-prompt D^0 the impact parameter distributions of all prompt D^0 and the reconstructed non-prompt D^0 are compared. For large D^0 impact parameters, the events in the prompt D^0 selection are dominated by non-prompt D^0 . Non-prompt D^0 with $\ln(IP_{D^0}) > -2.5$ are neglected. The selected subsample of non-prompt D^0 can be scaled with a constant factor such that the total number of events in the region of large D^0 impact parameters match. The decay time distributions for events with $\ln(IP_{D^0}) > -2.5$ in the whole dataset and the selected non-prompt subsample are shown in figure 6.11. They are normalized to the same number of events to compare the distributions.

A reasonable agreement is observed, which shows that this impact parameter region is dominated by non-prompt D^0 . Figure 6.12 shows the impact parameter distributions for all events from the prompt D^0 selection and the subsample of reconstructed non-prompt D^0 , together with the scaled subsample which has a similar shape as all prompt D^0 events in the region of high impact parameters.

This scaling factor accounts for the fact that only a small part of the non-prompt D^0 background can be reconstructed. It is found to be approximately equal to ≈ 50 . A modification of the impact parameter region where the factor is determined results in a variation of the scaling factor between 45 and 60, which can be taken into account as systematic uncertainty of the factor. In addition, the impact parameter significance, which is the D^0 impact parameter divided by its error, can be used to evaluate the scaling factor, which also leads to scaling factors within the same range.

The scaled subsample now represents the whole non-prompt D^0 background in RS events.

This allows to study the time-dependent fraction of non-prompt D^0 background within the signal and its dependence on different selection criteria. The decay time distribution is divided into several bins. In each bin, the number of D^0 (given by the reconstruction as prompt D^0) and the number of reconstructed non-prompt D^0 is counted. The latter one is then multiplied by the scaling factor to estimate the number of non-prompt D^0 in this bin. The division of the estimated non-prompt D^0 by the total number of D^0 gives the fraction of non-prompt background events in this bin. The result is shown in figure 6.13. The fraction is increasing with the D^0 decay time. After removing events with large D^0 impact parameter, the fraction gets significantly smaller.

6.3.5 Result

The reconstruction and selection of the non-prompt D^0 provides a way to get the distribution of the total non-prompt D^0 background in the RS data sample. In addition, it is possible to determine the fraction of non-prompt D^0 which are reconstructed. This allows to scale this sample to represent the full non-prompt D^0 background. The scaling factor is ≈ 50 and consistent with the expectation from the inclusive B Monte Carlo sample, as described in section 6.3.3. In the subsample of non-prompt D^0 , all parameters required for the analysis can be calculated in the event reconstruction:

- the wrongly assigned D^0 decay time from the reconstruction as prompt particle
- the true D^0 decay time from the reconstruction as non-prompt D^0 , up to measurement uncertainties
- the impact parameter of the D^0

This information enters a toy simulation which then allows to draw conclusions about the extraction of the mixing parameters (see section 8.2.1).

6.3.6 Correction of the bias on mixing parameters

The selection of semileptonic $\overline{B^0} \rightarrow D^* \mu \nu_\mu$ decays provides a way to estimate the non-prompt D^0 background in RS events. While it would be in principle possible to apply the same method for WS events, the size of the sample is not sufficient to use it. Due to mixing, the number and D^0 decay time dependence of non-prompt WS D^0 events is different from non-prompt RS D^0 events, but connected via the time-dependent ratio of WS to RS decays. Therefore, it is possible to calculate the decay time dependent rate of non-prompt WS events with the reconstructed non-prompt RS events. The calculation can be found in appendix A.3. The D^0 mixing parameters are required for this calculation, and the correction of the non-prompt D^0 background influences the determination of these mixing parameters.

An iterative method can be chosen to take this into account: As a first step, the non-prompt D^0 background is ignored and an estimate of the mixing parameters is calculated. This estimate is then used to calculate the bias on the mixing parameters from non-prompt D^0 and correct the WS/RS ratio accordingly. The new ratios are used to determine new, improved mixing parameters, which are used to improve the correction of the bias from non-prompt D^0 . These steps are repeated until the mixing parameters and the corrections due to non-prompt D^0 are stable. As the total fraction of non-prompt D^0 is much smaller than 1 and many B-mesons have a short decay time, the correction is small compared to the absolute value of the mixing parameters. This means that already the first determination of the mixing parameters allows a good approximation of the correction due to non-prompt D^0 , which leads to more precise mixing parameters afterwards. The method converges to the physical mixing parameters with the right correction for non-prompt D^0 .

The reconstruction of non-prompt D^0 allows to estimate the influence of the non-prompt D^0 background on the determination of mixing parameters. In the analysis of the 2011 dataset which is currently performed this method will have an important impact.

The dataset taken in 2010 is not large enough to perform this type of reconstruction. Nevertheless, the dataset of 2010 allows the determination of a time-integrated ratio of WS to RS decays, which is presented in the following chapter.

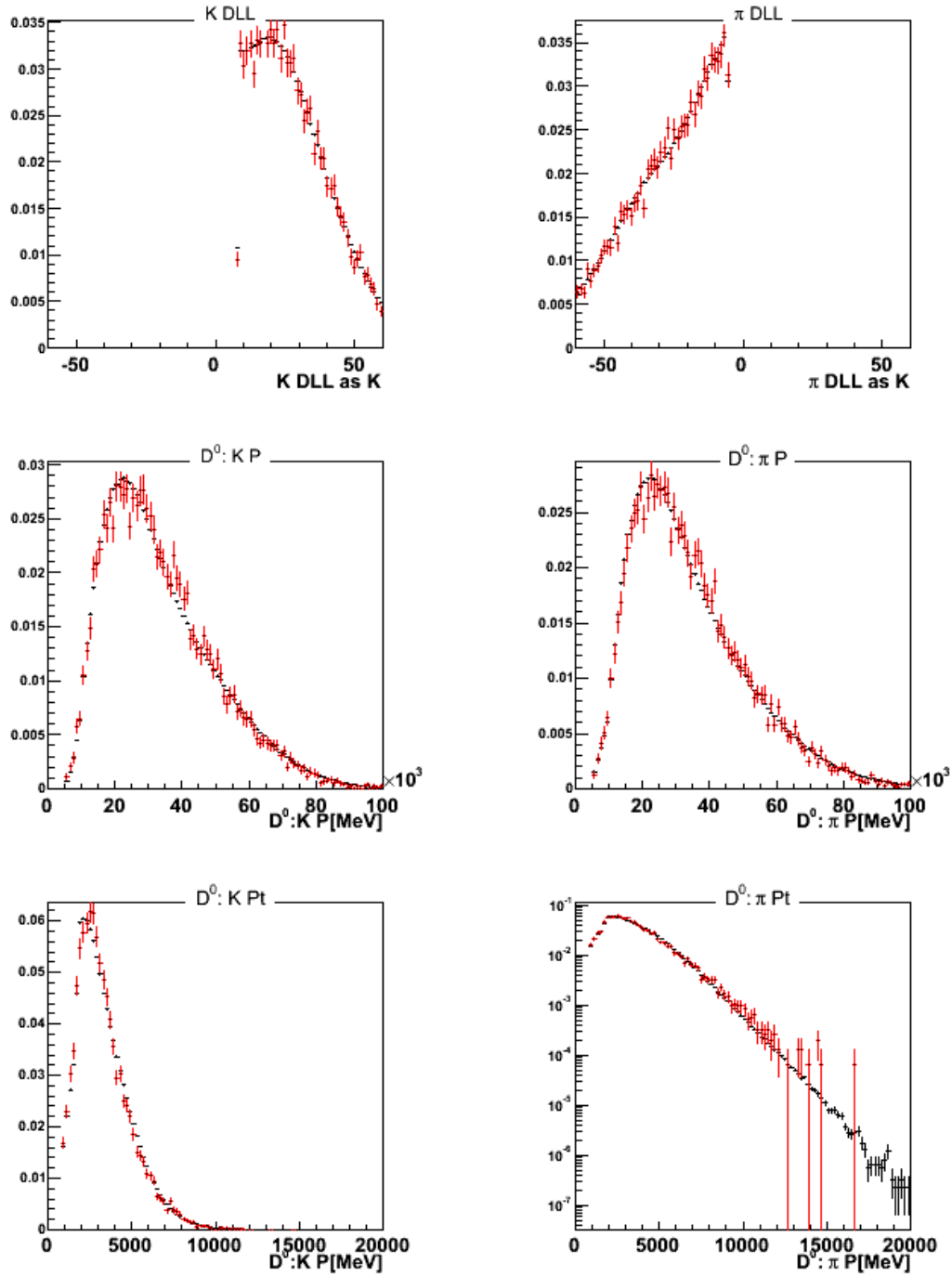


Figure 6.5: Comparisons between the D^0 daughters for all selected D^0 (black) and the non-prompt D^0 subsample (red), normalized to 1. The upper row shows the DLL distributions for kaons (left) and pions (right) as D^0 daughters. The DLL value is defined in section 4.4.4. The momentum (middle row) and transverse momentum (lower row) agree for both kaons (left) and pions (right), indicating that there is no kinematic difference between the two samples apart from the D^0 decay time, impact parameter and related variables.

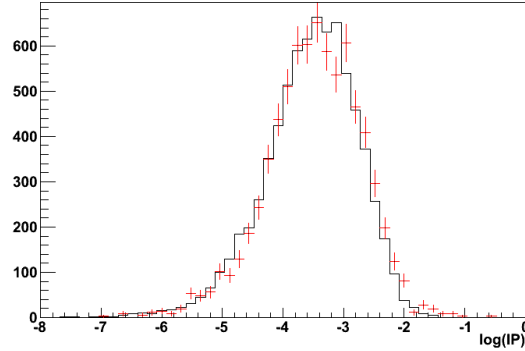


Figure 6.6: *Distribution of the logarithm of the impact parameter ($\log(IP)$) of D^0 from $\bar{B} \rightarrow D^* \mu \nu_\mu$ (black) compared with the $\log(IP)$ of D^0 from all other inclusive B decays (red), normalized to the same number of events. No significant difference can be seen.*

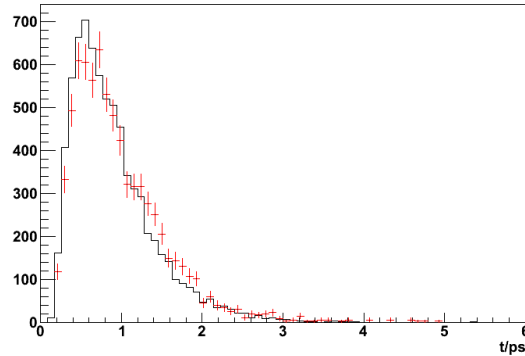


Figure 6.7: *Distribution of the D^0 decay time for simulation of $\bar{B} \rightarrow D^* \mu \nu_\mu$ (black) compared with a simulation of all other inclusive B decays (red), normalized to the same number of events. The graph shows the good agreement between both.*

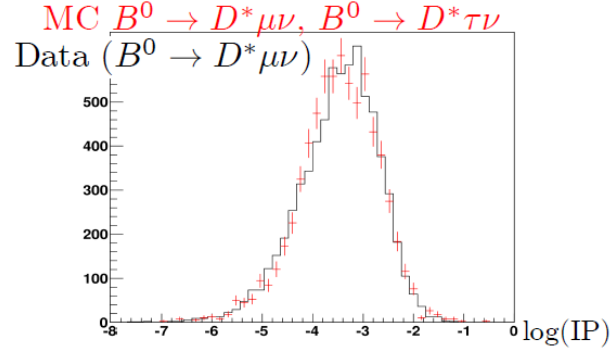


Figure 6.8: Distribution of the logarithm of the D^0 impact parameter for data (black) compared with the logarithm of the impact parameter in simulated events of $\bar{B} \rightarrow D^* \mu \nu_\mu$ (red), normalized to the same number of events. Both samples show a reasonable agreement.

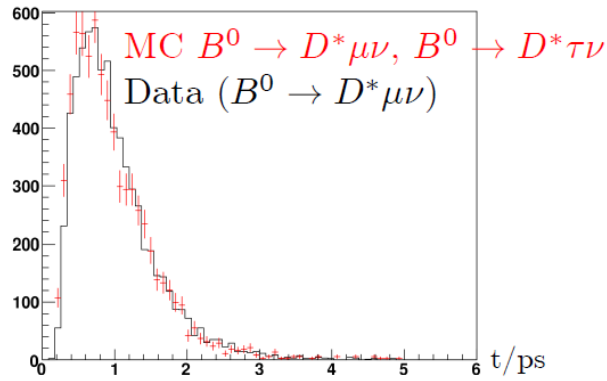


Figure 6.9: Distribution of the D^0 decay time for data (black) compared with a simulation of $\bar{B} \rightarrow D^* \mu \nu_\mu$ (red), normalized to the same number of events. The average decay time in the data sample is about $3\% \pm 1.5\%$ larger than in the simulation.

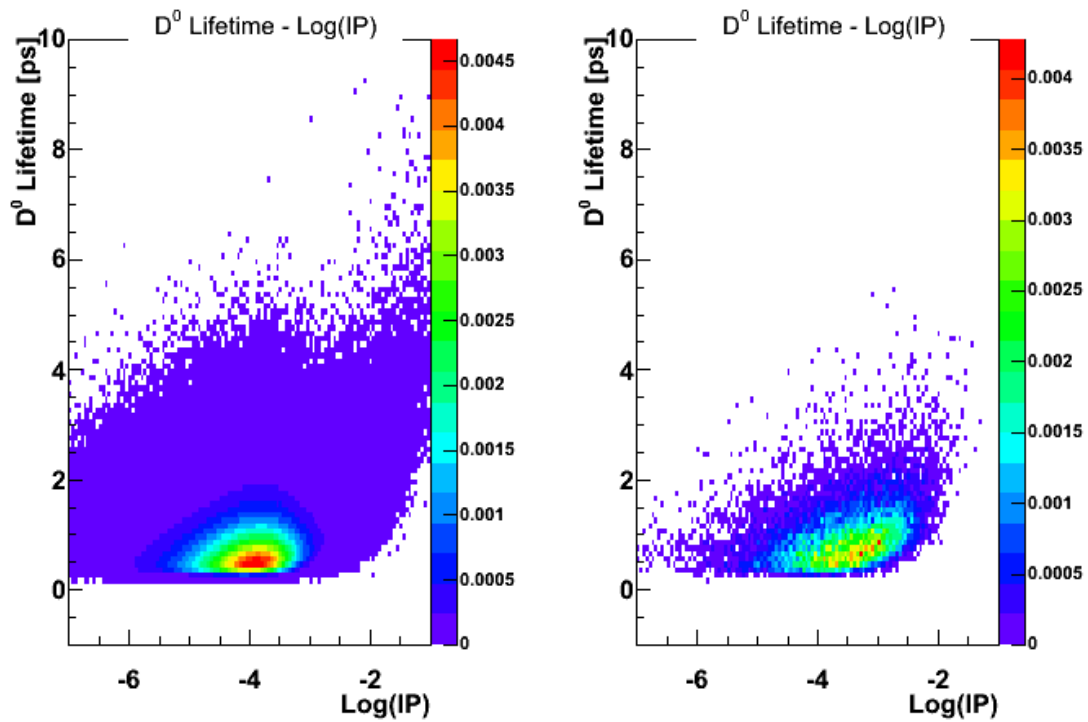


Figure 6.10: Two-dimensional distribution of (impact parameter, D^0 decay time) of all selected D^0 (left) and the non-prompt D^0 subsample (right). A shift towards higher impact parameter and higher reconstructed decay time is observed.

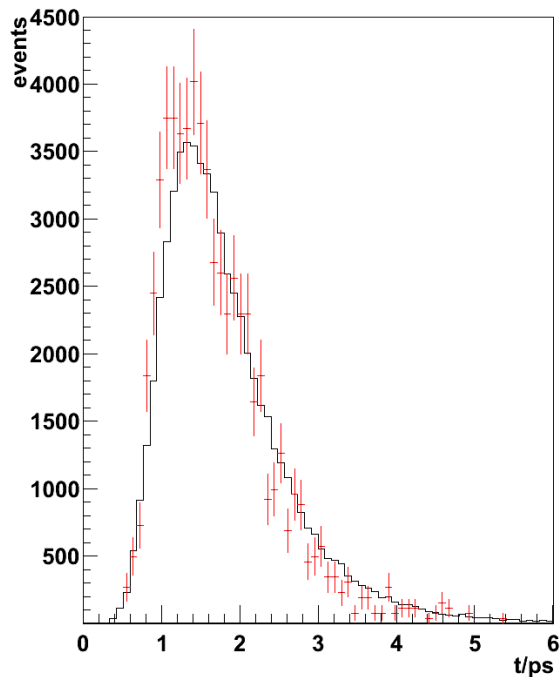


Figure 6.11: *Distribution of the reconstructed D^0 decay time for events with $\ln(IP_{D^0}) > -2.5$ for the whole dataset (black) compared with the selected non-prompt events (red), normalized to the same number of entries. The distributions are similar, showing that the region of high D^0 impact parameters is dominated by non-prompt D^0 .*

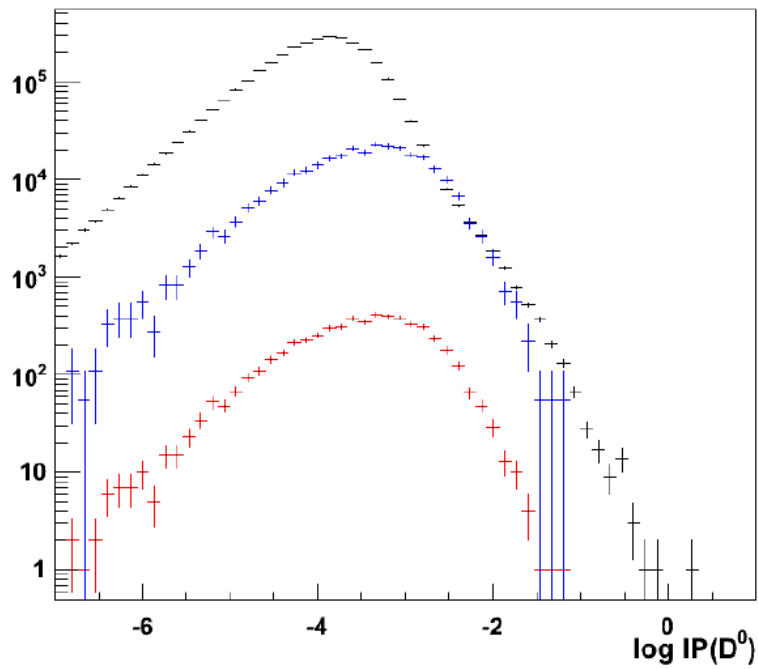


Figure 6.12: Distributions of the logarithm of the D^0 impact parameter for the total dataset (black) and the unscaled (red) and scaled (blue, factor 50) non-prompt D^0 subsample, as described in 6.3.4. For $\ln(IP) > -1.5$, the size of the non-prompt dataset is too small to appropriately describe the shape and statistical fluctuations are very large.

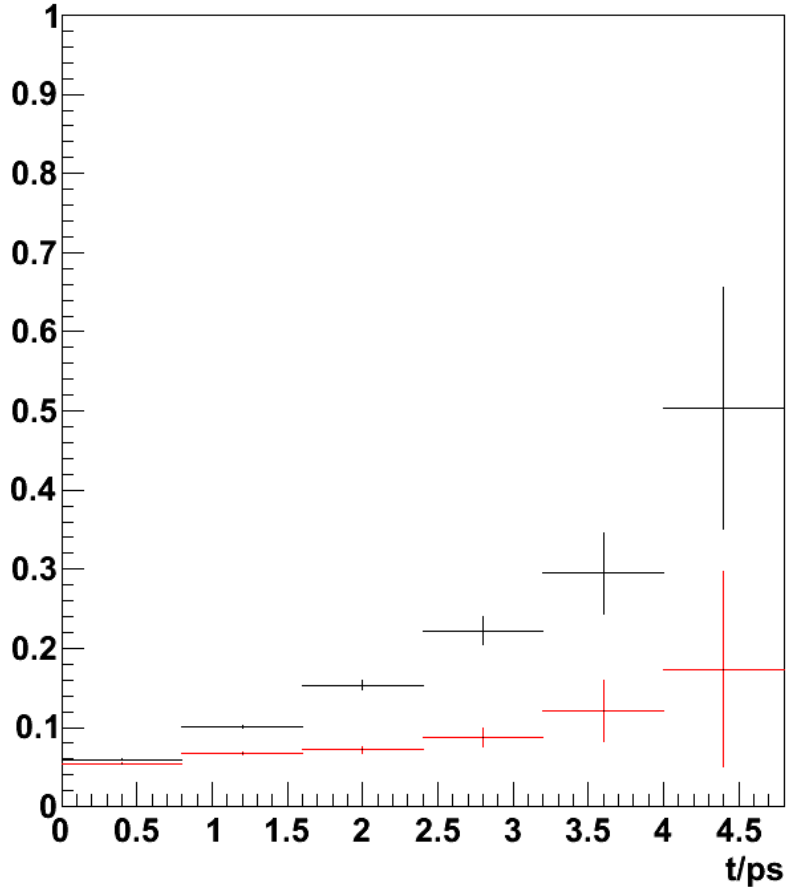


Figure 6.13: Time-dependence of the fraction of non-prompt D^0 in the dataset, before (black) and after (red) application of a selection on the D^0 impact parameter. The x-axis is the decay time in ps, the y-axis the fraction of non-prompt D^0 . The fraction of non-prompt D^0 increases with time, but the selection of events with a logarithm of the D^0 impact parameter of $\ln(IP_{D^0}) < -3$ can reduce this trend. The rightmost bin corresponds to D^0 with a decay time (as prompt particles) of 10 to 12 D^0 lifetimes.

Time-integrated ratio

As preparation for the time-dependent mixing measurement, the time-integrated ratio of WS to RS decays is determined with data corresponding to an integrated luminosity of $\int \mathcal{L} dt = (36.4 \pm 3.6) \text{pb}^{-1}$ taken in 2010 [28]. In total, 287038 RS and 34997 WS signal candidates are selected. A measurement of the time-integrated ratio with the dataset of 2011 is not available yet. This dataset is not large enough to extract mixing parameters, but the result shows that LHCb is able to perform this kind of measurements.

The measurement has several differences compared to the time-dependent mixing measurement which are discussed in this chapter. The result is presented and compared with the world average.

7.1 Modified fit method

Due to trigger settings during the data-taking period of 2010, events in the D^0 mass sidebands around the signal peak are removed already at trigger level, and the default two-dimensional fit to the signal and all background components, as described in section 5.2, is not possible. Because of the missing sidebands the fitting procedure cannot distinguish between signal events and misreconstructed background events.

A signal box is defined as $1849 \text{ MeV} < m(D^0) < 1879 \text{ MeV}$ and $144.32 \text{ MeV} < \delta m < 146.52 \text{ MeV}$, where the δm range corresponds to about ± 2 standard deviations from the mean value.

The D^0 mass range in the two-dimensional fit is reduced to the signal box, where the trigger acceptance is nearly independent of the D^0 mass. The sum of two gaussian distributions for the D^0 mass distribution is used to describe the signal and the random π_s background, the combinatorial and the misreconstructed background are not included in the fit.

Therefore, the fit function described in section 5.2 is simplified to

$$\mathcal{P}(m_{D^0}, \delta m) = \mathcal{P}_{mass}(m_{D^0}) \cdot (N_{signal} \cdot \mathcal{P}_{signal}(\delta m) + N_{slowpi} \cdot \mathcal{P}_{slowpi}(\delta m)) \quad (7.1)$$

with

$$\mathcal{P}_{mass}(m_{D^0}) = q_1 f_G(m_{D^0}, \overline{m}_{D^0}, \sigma_1) + (1 - q_1) f_G(m_{D^0}, \overline{m}_{D^0}, \sigma_2) \quad (7.2)$$

$$\mathcal{P}_{signal}(\delta m) = p_1 [p_2 f_G(\delta m, \overline{\delta m}_1, \sigma_{\delta m,1}) + (1 - p_2) f_G(\delta m, \overline{\delta m}_1, \sigma_{\delta m,2})] + (1 - p_1) f_G(\delta m, \overline{\delta m}_2, \sigma_{\delta m,3}) \quad (7.3)$$

and

$$\mathcal{P}_{slowpi}(\delta m) = f_{DstD0BG}(\delta m) = \left(\frac{\delta m}{A} \right)^2 \left(1 - e^{-\frac{\delta m - D}{C}} \right) + B \left(\frac{\delta m}{D} - 1 \right) \quad (7.4)$$

where $f_G(x, \bar{x}, \sigma)$ denotes a gaussian distribution with mean value \bar{x} and standard deviation σ .

The one-dimensional projections of the two-dimensional fit are shown in figures 7.1 for RS events and 7.2 for WS events. The pull distributions (small graphs) show the difference between data and the fit function, normalized to the statistical error of the data in each bin. For RS events, there are deviations in the δm distribution visible within the signal range. They are treated as systematic uncertainty and discussed in section 7.2. Apart from this, a good description of the signal is obtained.

Raw yields for signal (S_{raw}) and background (BG_{raw}) within the signal box are determined by integrating the two components of the fit function within the signal box.

In addition to the specific D^0 trigger which has removed the D^0 mass sidebands in 2010, D^0 are also present in events triggered by other particles and therefore independent of the D^0 and its reconstructed mass. These events can be used to estimate the level of misreconstructed and combinatorial background. There, the trigger does not influence the background shapes, but this unbiased dataset is much smaller. For these events which are within the signal region for δm , the D^0 mass distribution is fitted with a function \mathcal{P} which is the sum of a gaussian distribution for the signal and π_s background and a linear model for the combinatorial and misreconstructed background.

$$\mathcal{P}(m_{D^0}) = N_1 \cdot f_G(m_{D^0}, \overline{m}_{D^0}, \sigma) + a \cdot m_{D^0} + b \quad (7.5)$$

The fit is shown in figure 7.3, data and the fitted function show a good agreement. N_{Sig} and N_{BG} and their uncertainties are then obtained via integration of the

gaussian distribution and the linear model, respectively, over the signal box in the D^0 mass. Using these numbers, the background fraction $K = N_{BG}/(N_{Sig} + N_{BG})$ in the D^0 mass distribution can be calculated both for RS and WS events. The uncertainty on K is obtained with gaussian error propagation:

$$\Delta K = \frac{N_{Sig} \Delta N_{BG} \oplus \Delta N_{Sig} N_{BG}}{(N_{Sig} + N_{BG})^2} \quad (7.6)$$

where \oplus refers to quadratic summation, $a \oplus b = \sqrt{a^2 + b^2}$. The uncertainty is dominated by ΔN_{BG} , the correlation between N_{Sig} and N_{BG} is neglected.

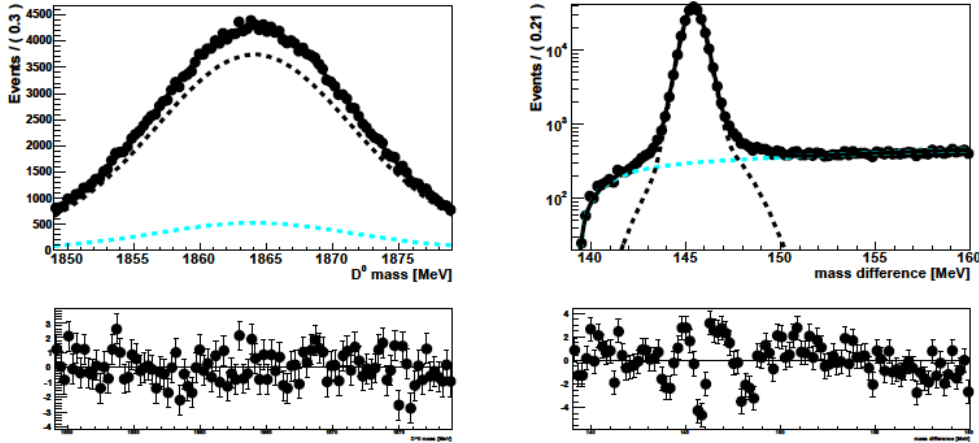


Figure 7.1: Projections to D^0 mass (left) and δm (right) of the two-dimensional fit of RS events. Signal is black, random slow pion background is cyan. The lower graphs show the pull distributions, that is the deviation between data and fit function, normalized to the statistical error of the data in each bin. The deviations visible in the δm projection are taken into account as systematic uncertainty.

The results of the two-dimensional fit to the full dataset and the one-dimensional fit to the unbiased dataset are then combined to subtract the background in the signal region and to get a corrected signal yield $S_{cor} = S_{raw} - K \cdot (S_{raw} + BG_{raw})$. This is done both for RS and WS events. The three variables are nearly uncorrelated, therefore the uncertainty of S_{cor} is given by

$$\Delta S_{cor} = (1 - K)\Delta S_{raw} \oplus K\Delta BG_{raw} \oplus (S_{raw} + BG_{raw})\Delta K \quad (7.7)$$

The values are shown in table 7.1. Using this signal yields, a ratio of WS to RS decays of $R = \frac{S_{cor}^{WS}}{S_{cor}^{RS}} = (0.442 \pm 0.033)\%$ is calculated. The uncertainty given here is statistical only. WS and RS events are uncorrelated, therefore

$$\frac{\delta R}{R} = \frac{\delta S_{cor}^{WS}}{S_{cor}^{WS}} \oplus \frac{S_{cor}^{RS}}{S_{cor}^{RS}} \quad (7.8)$$

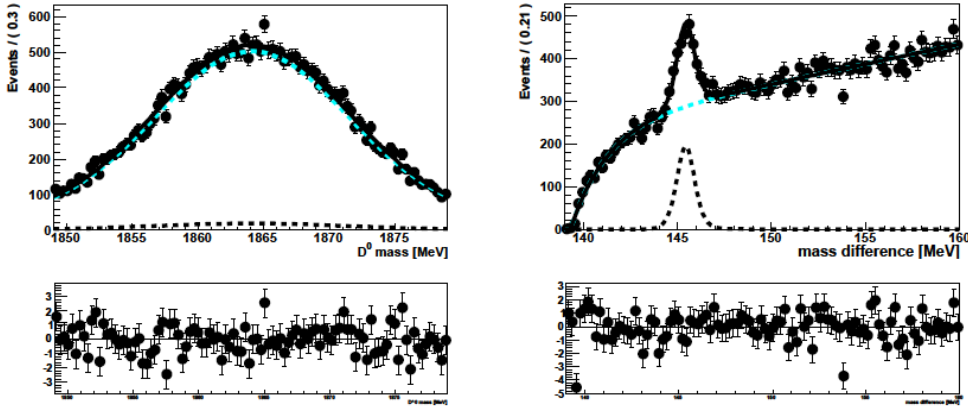


Figure 7.2: Projections of the two-dimensional fit of WS events. Signal is black, random slow pion background is cyan. The δm graph here has a linear y-scale, where it is logarithmic for RS events. The signal to background ratio is much smaller than for RS events.

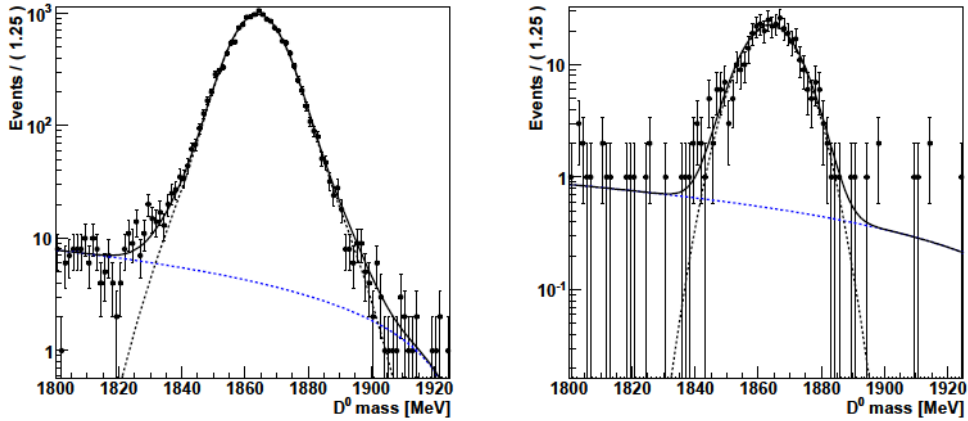


Figure 7.3: One-dimensional fit of the D^0 mass distribution within the signal region for RS (left) and WS decays (right). All events are triggered independently of the signal decay in order to study the D^0 mass sidebands. K , the background fraction in the signal region, can be determined from the fit results.

7.2 Systematic uncertainties

To evaluate systematic uncertainties, the fit model and the δm signal range are modified in both fits: A parabola is tested for the misreconstructed background in the one-dimensional D^0 RS mass fit, which modifies the value K to $K = 0.0052$, 22% less than the value obtained with a linear shape. The WS signal has not enough events for this. $\pm 22\%$ relative to the default value are used as systematic

	S_{raw}	BG_{raw}	K	S_{cor}
WS	1095 ± 66	3007 ± 18	0.0358 ± 0.0069	948 ± 70
RS	215976 ± 480	3165 ± 25	0.0066 ± 0.0006	214523 ± 494

Table 7.1: *Uncorrected and corrected signal yields for the 2010 dataset. Gaussian error propagation is used to calculate the uncertainties. BG_{raw} is the expected number of background events in the signal region, and its uncertainty is the uncertainty of this expectation, therefore it can be smaller than the square root of the value.*

uncertainty for K both for RS and WS events. This modifies the ratio R by $\Delta R = \pm 0.015\%$.

As alternative shape of the π_s background in the two-dimensional fit, a third order polynomial is used. R changes by 0.013% to $R = 0.428\%$. Other variations of the shapes give only negligible changes in the signal yields. The difference between the shape of the data and the fit function, which can be seen in figure 7.1, is evaluated within the signal box: In each bin, the absolute difference between data and fit is calculated and added for all bins with disagreement. This results in ≈ 3600 RS events. A variation of the RS signal yield by ± 3600 events modifies R by $\pm 0.007\%$, which is used as systematic uncertainty.

The full differences between the results with these variations and with the default fit method are taken as systematic uncertainty. As they are not uncorrelated, a conservative estimate is used and they are added linearly to an uncertainty of $\Delta R_{fit} = 0.035\%$ of the fitting method.

The δm signal range is increased to ± 3 standard deviations and a new ratio R is evaluated using this larger range and the default fit method described above, the difference $\delta R_{signalrange} = |0.419\% - 0.442\%| = 0.023\%$ is treated as systematic uncertainty. δm signal boxes outside the range of ± 2 to ± 3 standard deviations are not useful, as they remove too many signal events or include too many background events in the signal box, both increases the statistical fluctuations of the WS to RS ratio.

Both uncertainties are added in quadrature and yield the total systematic uncertainty of $\delta R = 0.042\%$.

7.2.1 Double misidentification

As described in section 5.3, D^0 mesons where both daughters are misidentified to fake a WS decay from a RS decay are suppressed with the mass exchange method. To study the effect of the remaining misidentified D^0 mesons, the ratio of WS to RS decays is extracted from a dataset where only the events which are removed by the method are used. The difference between the ratios is found to

be $R^{no\ massex} - R = 0.016\%$. The mass exchange method removes 98% of the misidentified background. As shown in appendix A.1, this method reduces the influence of double misidentified events on the measured R to $\approx 0.6\%$ of the difference $R^{no\ massex} - R$, therefore the uncertainty from these events is neglected.

7.3 Lifetime acceptance correction

The ratio of WS to RS decays is increasing with the D^0 lifetime. The requirement of minimal impact parameters for the D^0 daughters prefers D^0 mesons with larger decay times, where the physical WS to RS ratio is larger. This influences the measurement of the time-integrated ratio. Therefore, a correction has to be applied to the measured ratio in order to get the real ratio of WS to RS decays.

A re-weighting of the events is not feasible, as the acceptance is nearly zero for short D^0 decay times ($t_{D^0} < \frac{\tau_{D^0}}{2}$) and very small for $t_{D^0} < \tau_{D^0}$. Therefore, a re-weighting would lead to large weights of events with short D^0 decay time and large uncertainties of the WS to RS ratio.

To determine a relative decay time acceptance function $\epsilon(t)$, an exponential function is fitted to the measured decay time distribution of RS D^0 events, where the decay constant is fixed to the world average given by the PDG [4]. The ratio of the measured number of events divided by the exponential function provides an approximation for the decay time acceptance [29].

$\epsilon(t)$ is parameterized by $\epsilon(t) = p_0 - (p_1 t e^{p_2 - t p_3} - p_4 e^{p_5 - t p_3})^2$ with t in ps , the graphs are shown in figure 7.4. The fit function provides a good approximation to data. $\epsilon(t)$ has more parameters than necessary, but this parameterization improves the stability of the fit. The fit results are shown in table 7.2. The errors on the fit parameters are negligible.

Parameter	value
p_0	1.011
p_1	8.001
p_2	2.277
p_3	0.934
p_4	1.348
p_5	0.199

Table 7.2: *Fit results for the D^0 decay time acceptance. The function is defined in section 7.3.*

Using the physical ratio of the number of RS to WS decays (see chapter 2)

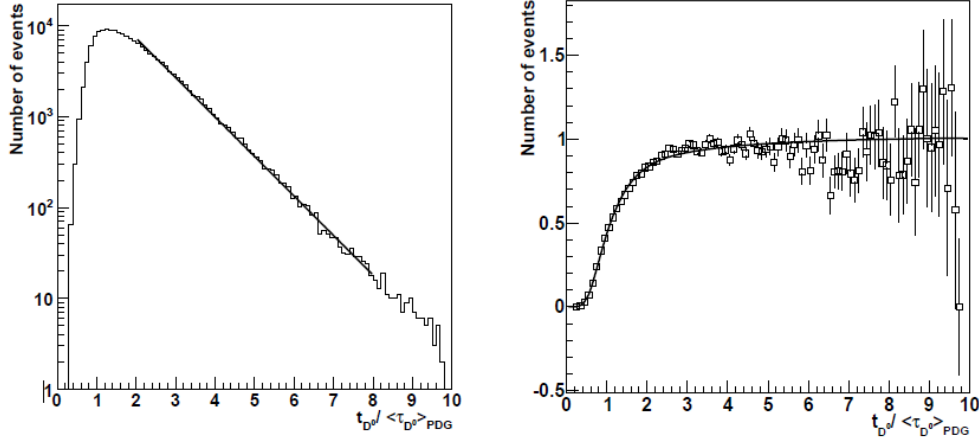


Figure 7.4: D^0 lifetime distribution of selected events (left) and a relative lifetime-dependent acceptance (right), determined on data. The full line in the left graph shows an exponential decay with the D^0 lifetime, the line in the right graph shows the determined $\epsilon(t)$. Taken from [29].

$$\begin{aligned} \frac{\int N_{WS}(t)dt}{\int N_{RS}(t)dt} &= \frac{\int e^{-\Gamma t} \left(R_{DCS} + \sqrt{R_{DCS}y'}\Gamma t + \frac{x'^2+y'^2}{4}(\Gamma t)^2 \right) dt}{\int e^{-\Gamma t} dt} \\ &= R_{DCS} + \sqrt{R_{DCS}y'} + \frac{x'^2 + y'^2}{2} \end{aligned} \quad (7.9)$$

and the measured ratio

$$\frac{\int N_{WS,meas}dt}{\int N_{RS,meas}dt} = \frac{\int \epsilon(t)N_{WS}dt}{\int \epsilon(t)N_{RS}dt} \quad (7.10)$$

a correction factor c_{acc} is defined as the physical WS to RS ratio divided by the measured WS to RS ratio:

$$c_{acc} := \frac{N_{WS}}{N_{RS}} / \frac{N_{WS,meas}}{N_{RS,meas}} = \frac{\int \epsilon(t)N_{RS}(t)dt}{\int \epsilon(t)N_{WS}(t)dt} \cdot \frac{\int N_{WS}(t)dt}{\int N_{RS}(t)dt} \quad (7.11)$$

The mixing parameters are taken of the Heavy Flavor Averaging Group, HFAG [30]. The evaluation of the integrals yields $c_{acc} = 0.926_{-0.045}^{+0.062}$, where the uncertainties of the mixing parameters are dominating. They are not included in the systematic uncertainty, as they do not come from the measurement itself.

In order to evaluate the true time-integrated ratio of WS to RS decays, the measured ratio is multiplied by c_{acc} .

7.4 Results

Figures 7.1 and 7.2 show the fits to RS and WS data. Table 7.3 shows the measured ratio of WS to RS decays R_{meas} and the acceptance corrected value $R_{cor} = R_{meas} \cdot c_{acc}$ together with the world average, as published by the PDG [4]. Within the uncertainties, R_{cor} and R_{PDG} show good agreement. As already pointed out, the main systematic uncertainties in the measurement are caused by the trigger limitations of the dataset of 2010, mainly the removed D^0 mass sidebands.

	N_{WS}/N_{RS} (%)
R_{meas}	$0.442 \pm 0.033(\text{stat.}) \pm 0.042(\text{sys.})$
R_{cor}	$0.409 \pm 0.031(\text{stat.}) \pm 0.039(\text{sys.})$
R_{PDG}	0.380 ± 0.018

Table 7.3: Measured and corrected time-integrated ratio of WS to RS decays with 2010 data, together with the world average.

Summary and Outlook

8.1 Summary

The LHCb experiment at the Large Hadron Collider (LHC) recorded proton-proton collisions at a center of mass energy of 7 TeV with an integrated luminosity of $\int \mathcal{L} dt = (36.4 \pm 3.6) \text{pb}^{-1}$ in 2010. This diploma thesis discusses the measurement of the time-integrated ratio of wrong sign (WS) $D^{*+} \rightarrow D^0(\rightarrow K^+\pi^-)\pi_s^+$ to right sign (RS) $D^{*+} \rightarrow D^0(\rightarrow K^-\pi^+)\pi_s^+$ decays. After applying selection criteria to enhance the purity of the WS D^0 decays, the number of WS and RS events is determined with a fit to the D^0 mass and the difference between the D^{*+} and the D^0 mass of the signal candidates. The mass exchange method (a method to test the D^0 daughter particle identification by recalculating the D^0 mass after exchanging the K and the π masses) is applied to remove misidentified D^0 and a background subtraction is performed to remove misreconstructed events. The systematic uncertainties in the determination of the number of WS and RS events are evaluated. The dominating uncertainties come from the trigger settings in 2010, as the D^0 mass sidebands were removed at the software stage of the trigger.

The decay time acceptance corrected ratio is measured to be

$$R = \frac{N_{WS}}{N_{RS}} = (0.442 \pm 0.033 \text{ (stat.)} \pm 0.042 \text{ (sys.)})\% \quad (8.1)$$

and consistent with the world average of

$$R_{\text{PDG}} = (0.380 \pm 0.018)\% \quad (8.2)$$

given by the Particle Data Group.

The number of 948 ± 70 WS D^0 decays in the 2010 dataset is not sufficient to perform a time-dependent analysis of the ratio of WS to RS decays to extract mixing parameters. However, the time-integrated measurement of the ratio shows that LHCb is able to perform an analysis of charm mixing with a larger dataset.

A method for a time-dependent mixing analysis and its challenges are discussed and solutions are presented to avoid systematic errors and to estimate uncertainties of the measurement. This includes asymmetries in the measurement and the different background components, especially a double misidentification of the D^0 daughters and non-prompt D^0 , which originate from decays of B mesons. As the reconstruction of the D^{*+} decay vertex has a large uncertainty, prompt D^{*+} from the primary vertex are used and the position of the primary vertex is assumed to be the D^{*+} decay vertex to calculate the D^0 flight distance and decay time. For D^{*+} mesons which are produced in the decay of B mesons, this leads to a wrong reconstruction of the D^{*+} decay vertex and therefore a wrong decay time measurement of the D^0 . This might influence the measurement of the time-dependent ratio of WS to RS decays, and therefore it has to be taken into account in the analysis. A new method to study the background from non-prompt D^{*+} on data is presented, based on a reconstruction of the decay channel $\bar{B} \rightarrow D^{*+}\mu^-\nu(X)$. It is shown that events in this decay channel are representative for the whole non-prompt background from B mesons. This allows to estimate the influence of non-prompt D^{*+} on the measured mixing parameters without Monte Carlo simulations. Selection criteria for that decay channel are developed, and the resulting sample of non-prompt events is compared to Monte Carlo simulations, with good agreement between both. A possibility to determine the fraction of non-prompt D^{*+} and the error of the D^0 decay time measurement in these events is illustrated, and a new method to correct their influence on the analysis of the charm mixing parameters is presented.

8.2 Outlook

The dataset recorded by LHCb in 2011, corresponding to 1.04 fb^{-1} , will allow to perform a time-dependent analysis of the WS $D^0 \rightarrow K^+\pi^-$ to RS $D^0 \rightarrow K^-\pi^+$ ratio. The number of RS signal candidates passing all selection criteria amounts to $1.1 \cdot 10^7$. The time-dependent measurement of the WS to RS D^0 decay ratio is expected to increase precision on the mixing parameters of the charm system. In particular, it enters a global fit [30] of mixing parameters allowing for CP-violation and can help to interpret experimental results in the charm system, most notably the recent LHCb result of ΔA_{CP} [8].

8.2.1 Toy MC study

A toy Monte Carlo study is currently performed to investigate the possibility to measure the mixing parameters R_D , y' and x' with the dataset collected in 2011 [31]. The simulation includes the RS and WS decay time distributions together with a gaussian resolution function for the D^0 decay time and a background component of non-prompt D^0 decays. As decay time acceptance, the function de-

terminated in section 7.3 is used. In case of toy experiments with D^0 s from B meson decays, additional exponential decays are simulated for a fraction of the events. In the toy simulation, the effective lifetime $\tau_{B^0} = 0.22\text{ps}$ and fraction f_{B^0} of B mesons is taken as measured in data. This is significantly shorter than the true lifetime of B mesons and accounts for the selection criteria on the D^0 topology, which favour short-living B mesons. The parameters used to simulate the mixing according to equation (2.10) are shown in table 8.1.

Simulation Parameter	values
D^0 decay time	0.410 ps
decay time resolution	0.045 ps
R_D	0.003
y'	0.001
x'	0.001
fraction of the non-prompt D^0 decays	5.3 %
effective B lifetime	0.22 ps
number of events	$7 \cdot 10^6$

Table 8.1: *Parameters of the toy MC simulation.*

The number of simulated RS events is $\approx 7 \cdot 10^6$, which corresponds to the dataset collected in 2011 after removing events with a large impact parameter. Non-equidistant bins are defined and the number of WS and RS events in each bin is determined. The ratio is then calculated in each bin. Figure 8.1 shows the result of a single simulation as green symbols. The upper part is simulated without non-prompt D^0 and the lower part is generated with a fraction of 5.3 % non-prompt D^0 and a large effective B lifetime of 0.5 ps compared to the measurement of 0.15 - 0.22 ps depending on the fit range. The blue lines correspond to the mixing function calculated using the input parameters of the simulation. The red lines are the results of χ^2 fits of equation (2.10) to the simulated WS to RS ratios. The fit yields the D^0 mixing parameters $\sqrt{R_D}$, y' and x'^2 . While the distribution without D^0 mesons from B decays reproduces the input very well, the non-prompt D^0 component causes a systematic shift of x'^2 to smaller values. It should be noted that τ_{B^0} is a factor of three larger than measured in data in order to demonstrate the impact of the non-prompt D^0 component to the fit.

The quality of the time-dependent fit can be evaluated with pull distributions: the deviation between input parameter and fitted parameter is divided by the uncertainty of the fit parameter. If the fit is unbiased, a normalized Gaussian distribution is expected. Figure 8.2 shows the pull distributions of the mixing parameters for a set of about 700 toy experiments without non-prompt D^0 background. Within the uncertainties the pull distributions are Gaussian with mean zero and width one. Therefore, the fitting procedure is considered as unbiased.

As already indicated by figure 8.1 a component of non-prompt D^0 can influence the fitting results, depending on the fraction of these events and the effective

B lifetime. Figure 8.3 shows the pull distributions with a non-prompt component as determined on data. The dependence of the mean and width of the pull distributions on the effective B lifetime is shown in figure 8.4 for the mean and in figure 8.5 for the width. In the range of the value for the effective lifetime τ_{B^0} determined in data, no bias in the determination of the mixing parameters R_D , y' and x'^2 is found.

The toy study shows a high sensitivity to mixing parameters with the dataset recorded by LHCb in 2011. The influence of non-prompt background on the measured mixing parameters can be studied. Using the reconstructed non-prompt D^0 from data, it is indicated that a selection on the impact parameter as used by the toy study is sufficient to reduce this influence to a negligible level. Further checks are required to validate this result.

8.2.2 Possible future measurements

It is expected that in 2012 a larger dataset can be collected than in 2011. A better description of the lifetime acceptance may allow to measure mixing with a time-dependent fit, as described in section 5.1. Further improvements of the analysis could permit separate mixing measurements for D^0 and $\overline{D^0}$, which could constrain the rate of CP-violation in the charm system. However, this requires a good knowledge of detection asymmetries for $K^\pm\pi^\mp$.

The high rate of B-mesons detected in the LHC can allow to use D^0 from decays of B-mesons for a WS analysis. This avoids the random π_s background and therefore the main background in the WS sample. In addition, the production vertex of the D^0 can be reconstructed directly with good precision, which removes the issues arising in the analysis of prompt D^0 from D^{*+} . The decay channel $\overline{B^-} \rightarrow D^0\mu^-\nu(X)$ is the most promising channel for this analysis. The downside of this channel is the requirement of a precise knowledge of the mistagging probability, as a mistagged RS decay looks like a WS decay.

An even cleaner sample can be studied with the decay $\overline{B^0} \rightarrow D^{*+}\mu^-\nu(X)$, $D^{*+} \rightarrow D^0(\rightarrow K\pi)\pi_s^+$. The decay chain requires the reconstruction of four particles and the correct decay channels for $\overline{B^0}$, D^{*+} and D^0 at the same time, therefore the size of the dataset is smaller. This can be partially countered by looser selection criteria.

These measurements can be used to measure mixing in the charm system with several independent D^0 production channels and different analysis methods, which gives the possibility to significantly increase the accuracy of the determination of the mixing parameters.

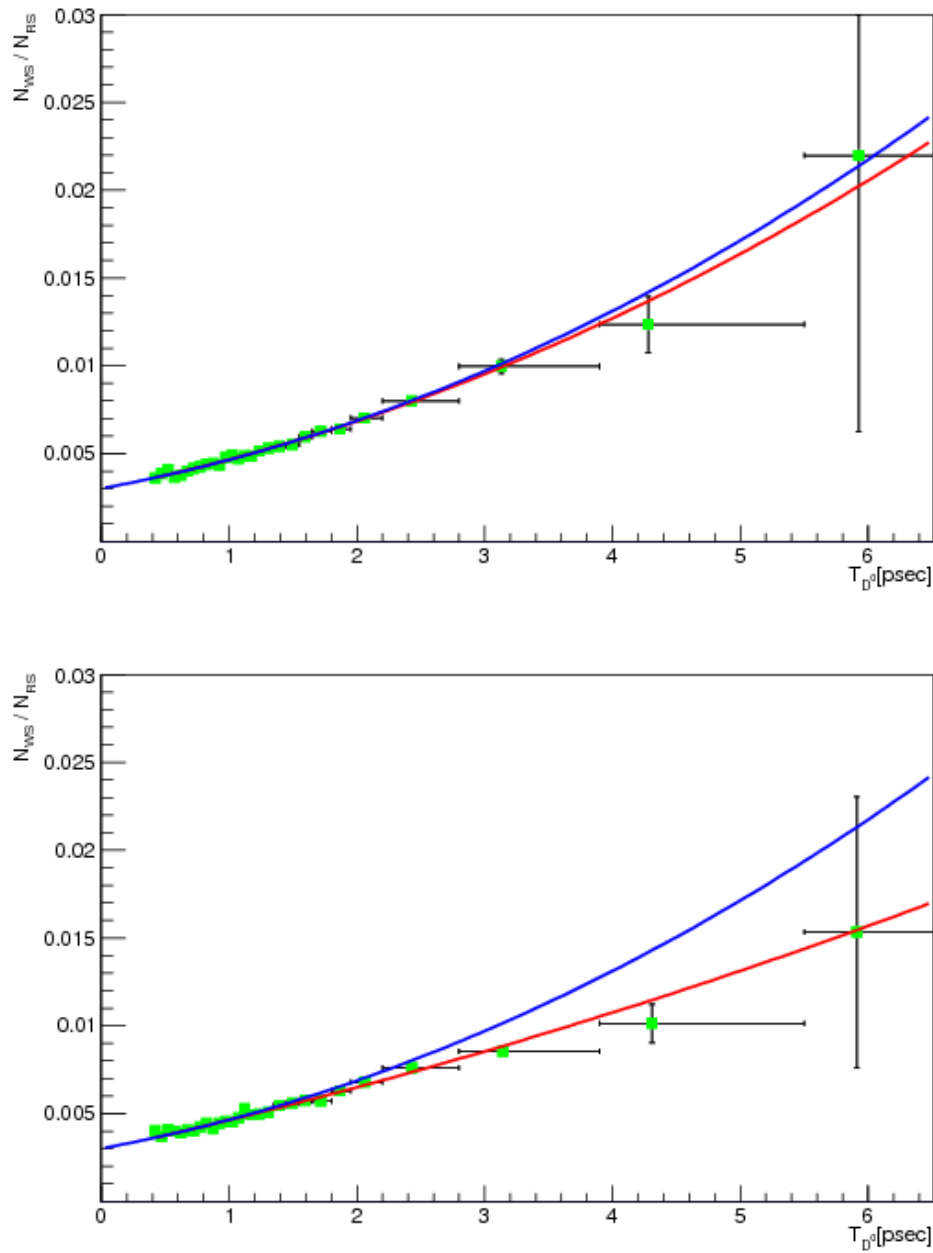


Figure 8.1: Fit of the D^0 decay time distribution to obtain mixing parameters (R_D , y' , x'^2) for a single toy experiment with about 7 million events after applying the LHCb decay time acceptance. Upper part: without non-prompt D^0 , lower part: with a fraction of 5.3% non-prompt D^0 with an effective B lifetime of 0.5 ps. The blue line corresponds to the simulation input and the red line is the result of the mixing fit. [31]

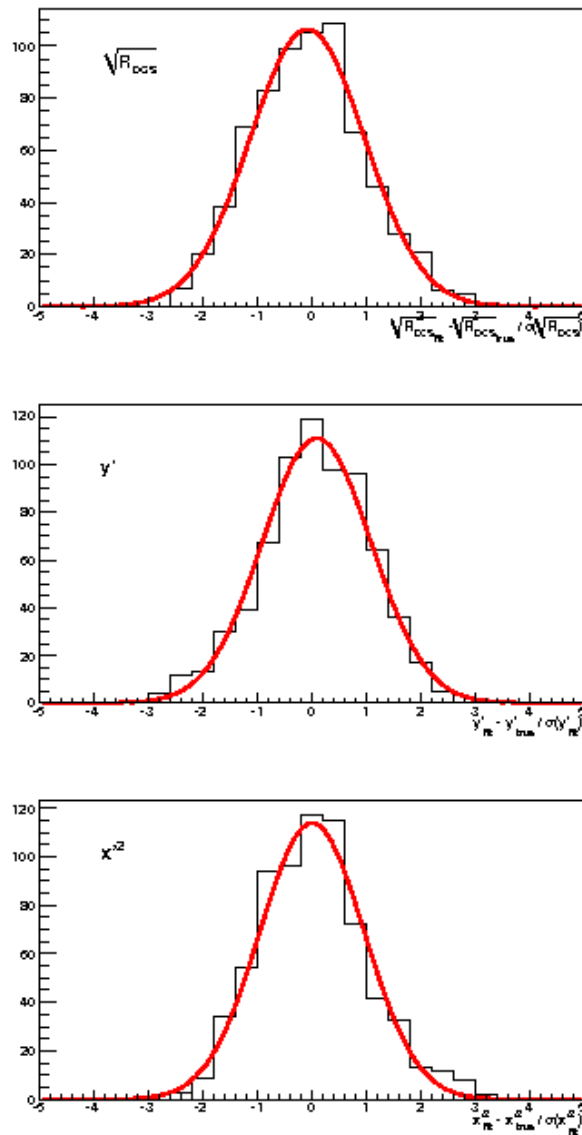


Figure 8.2: Pull distributions of the fit of the mixing parameters R_D , y' and χ^2 for a set of about 700 toy experiments with about 7 million events each, without non-prompt component. [31]

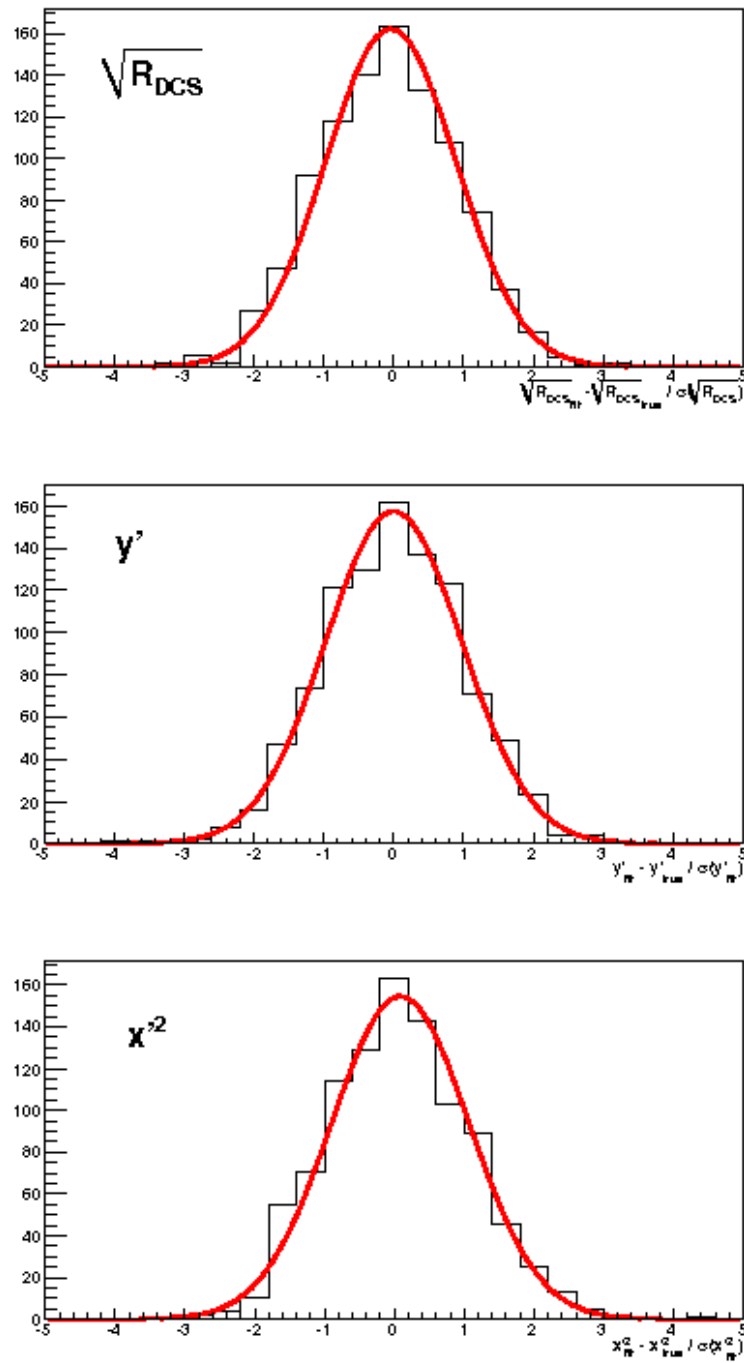


Figure 8.3: Pull distributions of the fit of the mixing parameters R_D , y' and x^2 for a set of about 700 toy experiments with about 7 million events each, with a non-prompt component as determined on data. [31]

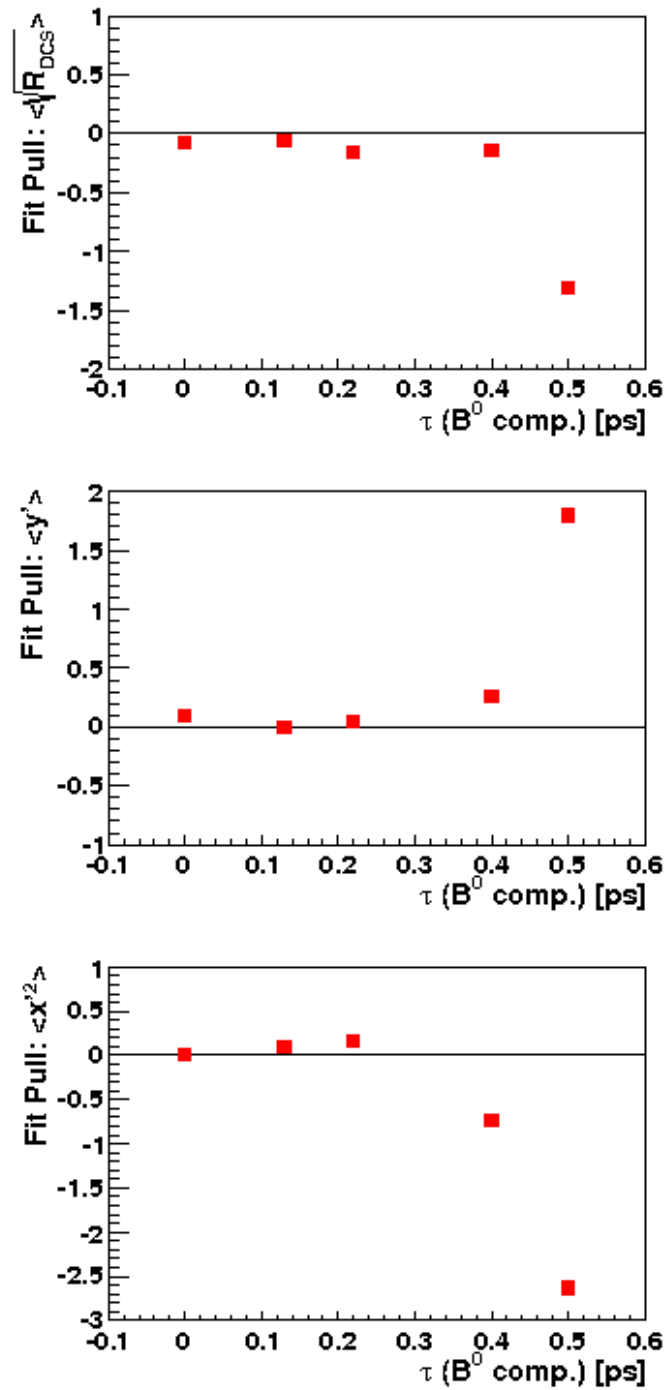


Figure 8.4: Mean values of pull distributions of the mixing parameters R_D , y' and x'^2 , depending on the effective B lifetime. [31]

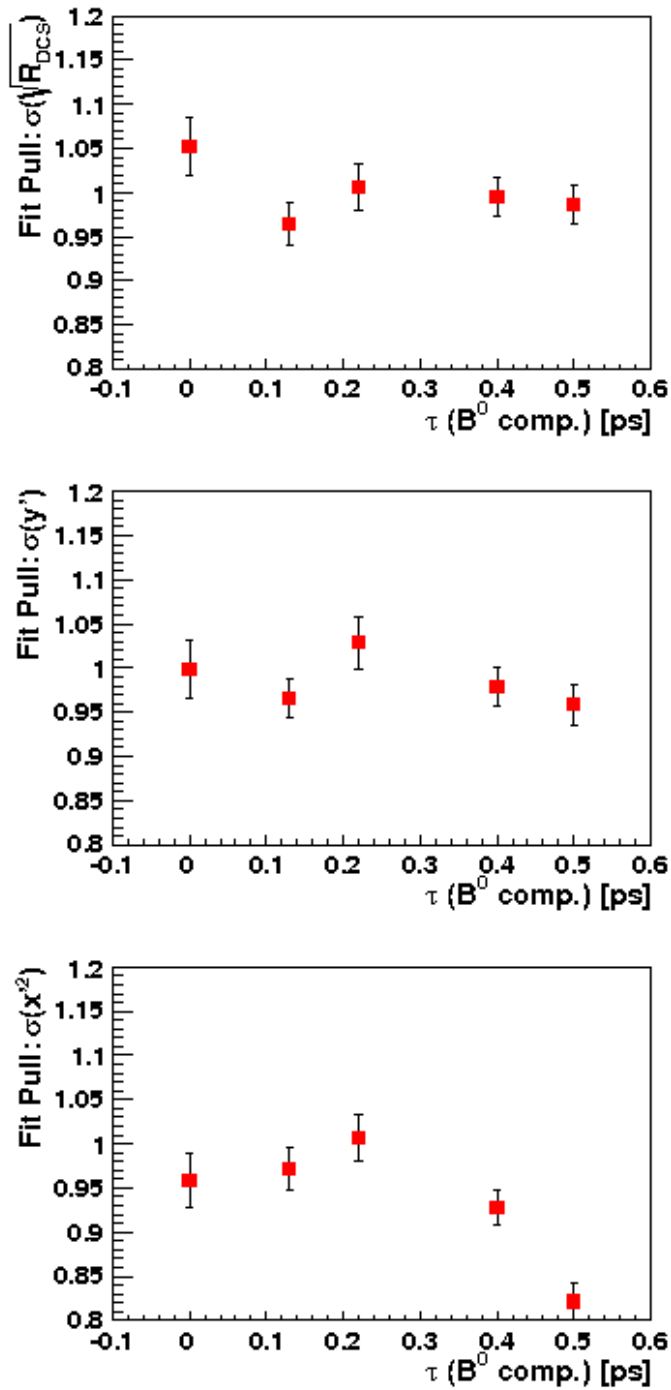


Figure 8.5: Widths of pull distributions of the mixing parameters R_D , y' and x'^2 , depending on the effective B lifetime. [31]

Appendix

A.1 Double misidentified events

Based on section 5.3.1: The probabilities $P_{right} = 98\%$ that a correct particle identification results in a mass within the signal box and $P_{wrong} = 23\%$ that a misidentification gives a mass within the signal box can be gained from RS data as shown in figure 5.2. Using these numbers, it is possible to evaluate the probability of a double misidentification, P_{misid} . In order to do this, the dataset is splitted in two samples: Events which are not removed by the mass exchange method and events which are removed. The former one contains three event categories:

- RS decays, reconstructed as RS: $p(RS \rightarrow RS) \propto (1 - P_{misid})P_{right}(1 - P_{wrong})$
- RS decays, reconstructed as WS: $p(RS \rightarrow WS) \propto P_{misid}P_{wrong}(1 - P_{right})$
- WS decays, reconstructed as WS: $p(WS \rightarrow WS) \propto (1 - P_{misid})P_{right}(1 - P_{wrong})$

Again, the misidentification of WS decays as RS is negligible. The first factor accounts for the particle identification, the second for the probability to find the events within the signal range for this identification, and the third factor is the probability that the event is not removed by the mass exchange method.

Using the time-integrated physical ratio R of WS to RS decays, it is possible to write down the measured ratio with the mass exchange method as

$$\begin{aligned}
 R^{massex} &= \frac{N_{WS}}{N_{RS}} \\
 &= \frac{Rp(WS \rightarrow WS) + p(RS \rightarrow WS)}{p(RS \rightarrow RS)} \\
 &= R + \frac{P_{misid}}{1 - P_{misid}} \frac{P_{wrong}}{1 - P_{wrong}} \frac{1 - P_{right}}{P_{right}}
 \end{aligned} \tag{A.1}$$

For events which are removed by the mass exchange method, the last factor for each category is different:

- RS decays, reconstructed as RS: $p(RS \rightarrow RS) \propto (1 - P_{misid})P_{right}P_{wrong}$
- RS decays, reconstructed as WS: $p(RS \rightarrow WS) \propto P_{misid}P_{wrong}P_{right}$

- WS decays, reconstructed as WS: $p(WS \rightarrow WS) \propto (1 - P_{misid})P_{right}P_{wrong}$

This can be translated into a different measured ratio of WS to RS events.

$$\begin{aligned}
R^{no\,massex} &= \frac{N_{WS}}{N_{RS}} \\
&= \frac{R p(WS \rightarrow WS) + p(RS \rightarrow WS)}{p(RS \rightarrow RS)} \\
&= R + \frac{P_{misid}}{1 - P_{misid}}
\end{aligned} \tag{A.2}$$

Both ratios can be measured on data. Using the difference, $R^{no\,massex} - R^{massex}$ and the values of P_{right} and P_{wrong} , it is possible to calculate

$$\frac{P_{misid}}{1 - P_{misid}} = (R^{no\,massex} - R^{massex}) \frac{1 - P_{wrong}}{P_{wrong}} \frac{1 - P_{right}}{P_{right}} \tag{A.3}$$

and the bias is then given by

$$R^{massex} - R = \frac{P_{misid}}{1 - P_{misid}} \frac{P_{wrong}}{1 - P_{wrong}} \frac{1 - P_{right}}{P_{right}} \tag{A.4}$$

Using the equations given above and $P_{right} = 98\%$ and $P_{wrong} = 23\%$, it is possible to calculate $R^{massex} - R$ as

$$\begin{aligned}
R^{massex} - R &= R^{no\,massex} - R^{massex} \cdot \frac{\frac{P_{wrong}}{1 - P_{wrong}} \frac{1 - P_{right}}{P_{right}}}{1 - \frac{P_{wrong}}{1 - P_{wrong}} \frac{1 - P_{right}}{P_{right}}} \\
&\approx 6.1 \cdot 10^{-3} \cdot (R^{no\,massex} - R^{massex})
\end{aligned} \tag{A.5}$$

A.2 Detection and production asymmetries

In principle, it is possible to determine and to remove D^0 production and detection asymmetries (see section 5.4.3) on data: The signal yields of RS and WS events can be determined for D^{*+} and D^{*-} separately, giving four values. Neglecting CP violation, these are related to four unknown parameters:

- the physical ratio of WS to RS events
- the production and π_s detection asymmetry
- the D^0 detection asymmetry
- a scale for the total number of events

The signal yields can be determined time-integrated or in each bin of time, and the equation system can be solved for the unknown parameters. However, this method has not been tested yet.

A.3 Influence of non-prompt D^0 on the WS to RS ratio

Using the dataset of reconstructed non-prompt RS D^0 (see chapter 6), it is possible to calculate the effect of non-prompt D^0 on the measured WS to RS ratios.

Let t be the reconstructed lifetime as prompt D^0 and let t' be the error of the lifetime measurement for non-prompt D^0 , such that $t - t'$ is the true D^0 lifetime. Errors in the lifetime measurement are not taken into account, as its influence on the non-prompt background is negligible.

Let $M(t)$ be the time-dependent physical ratio of WS to RS decays, as described in section 2.2:

$$M(t) = R_D + \sqrt{R_D y'} \cdot \Gamma t + \frac{x'^2 + y'^2}{4} \cdot (\Gamma t)^2 \quad (\text{A.6})$$

The time-dependent rate of RS decays can be split into prompt and non-prompt D^0 :

$$RS(t) = RS_p(t) + RS'_s(t) \quad (\text{A.7})$$

The non-prompt D^0 have a two-dimensional distribution in t and t' , the one-dimensional distribution can be obtained via integration:

$$RS(t) = RS_p(t) + \int_0^t dt' RS_s(t, t') \quad (\text{A.8})$$

The WS distribution is like the RS distribution, but with an additional factor of $M(t)$ with the true D^0 lifetime t :

$$WS(t) = M(t)RS_p(t) + \int_0^t dt' M(t - t')RS_s(t, t') \quad (\text{A.9})$$

At the right side of this equation, add $M(t)RS_s(t)$ to the first summand and subtract its integral representation from the integral:

$$WS(t) = M(t)RS_p(t) + M(t)RS_s(t) + \int_0^t dt' (M(t - t') - M(t))RS_s(t, t') \quad (\text{A.10})$$

Now, the sum of prompt and non-prompt RS decays can be written as the total number of RS decays.

$$WS(t) = M(t)RS(t) + \int_0^t dt' (M(t - t') - M(t))RS_s(t, t') \quad (\text{A.11})$$

This equation describes the usual mixing ($M(t)RS(t)$) together with a correction term. Using the equation for $M(t)$, it is possible to find a different expression for the correction:

$$\int_0^t dt' (M(t-t') - M(t)) RS_s(t, t') = \int_0^t dt' A_1 t' RS_s(t, t') + \int_0^t dt' A_2 t'^2 RS_s(t, t') \quad (\text{A.12})$$

with $A_1 = -\sqrt{R_D} y' \Gamma - 2t \frac{x'^2 + y'^2}{4} \Gamma^2$ and $A_2 = \frac{x'^2 + y'^2}{4} \Gamma^2$

Both A_1 and A_2 are independent of t' and can be moved out of the integrals. To calculate the correction, it is necessary to know $\int_0^t dt' t' RS_s(t, t')$ and $\int_0^t dt' t'^2 RS_s(t, t')$. This does not depend on any data for non-prompt WS D^0 . Therefore, the integrals can be calculated using the scaled sample of non-prompt RS events. In the binned method, $WS(t)$ is integrated within bins, the same can be done for the non-prompt D^0 to get $\int_0^t dt' t' RS_s(t, t')$ and $\int_0^t dt' t'^2 RS_s(t, t')$ for each bin of time by summing over the selected non-prompt D^0 events within this bin.

With mixing parameters as input, A_1 and A_2 can be calculated and the number of WS events in each bin of time can be corrected. This allows an iterative method to remove the bias from non-prompt D^0 on the mixing parameters.

Bibliography

- [1] T. Aaltonen et al. (CDF Collab.), ”*Evidence for $D^0 - \bar{D}^0$ mixing using the CDF II Detector*”, Phys. Rev. Lett. 100 (2008) 121802.
- [2] M. Staric et al. (Belle Collab.), ”*Evidence for $D^0 - \bar{D}^0$ Mixing*”, Phys. Rev. Lett. 98 (2007) 211803.
- [3] B. Aubert et al. (BaBar Collab.), ”*Evidence for $D^0 - \bar{D}^0$ Mixing*”, Phys. Rev. Lett. 98 (2007) 211802.
- [4] K. Nakamura et al. (Particle Data Group), J. Phys. G 37, 075021 (2010)
- [5] D.M. Asner et al. (CLEO Collaboration), ”*Determination of the $D^0 \rightarrow K\pi$ Relative Strong Phase Using Quantum-Correlated Measurements in $e^+e^- \rightarrow D^0\bar{D}^0$ at CLEO*”, Phys. Rev. D78 (2008) 012001.
- [6] M. Alexander et al., ”*Time-dependent analyses of two-body charm decays*”, LHCb internal note, CERN-LHCb-INT-2010-056, 2010
- [7] *No Pain, No Gain: On the Challenges and Promises of Charm Studies.* I.I. Bigi (Notre Dame U.). UND-HEP-09-BIG05. Jul 2009. 19 pp.
- [8] *Evidence for CP violation in time-integrated $D^0 \rightarrow h - h^+$ decay rates.* LHCb Collaboration (R. Aaij et al.), Dec 2011 [arXiv:1112.0938]
- [9] The LHCb Collaboration, *LHCb Technical proposal*, CERN-LHCC/98-4, 1998.
- [10] The LHCb Collaboration, *LHCb Velo technical design report*, CERN-LHCC/2001-011, 2001.
- [11] The LHCb Collaboration. *The LHCb Detector at the LHC.* JINST 3 S08005, 2008.

-
- [12] The LHCb Collaboration, *LHCb Silicon Tracker - Material for Publications*, 2010.
- [13] The LHCb Collaboration, *LHCb Inner Tracker design report*, CERN-LHCC/2002-029, 2003.
- [14] The LHCb Collaboration, *LHCb Outer Tracker Technical Design Report*, CERN/LHCC-2001-024, 2001.
- [15] The LHCb Collaboration, *LHCb RICH technical design report*, CERN-LHCC/2000-037, 2000.
- [16] The LHCb Collaboration, *LHCb Calorimeters Technical Design Report*, CERN/LHCC-2000-036, 2000.
- [17] The LHCb Collaboration, *LHCb Muon Technical Design Report*, CERN/LHCC-2000-037, 2000.
- [18] *The LHCb Simulation Application, Gauss: Design, Evolution and Experience*
M Clemencic et al 2011 J. Phys.: Conf. Ser. 331 032023
- [19] Sjstrand, T., et al., *PYTHIA*, Computer Physics Commun., 135 (238), 2001.
- [20] Ryd, A., et al., *EvtGen A Monte Carlo Generator for B-Physics*, BAD 522 v6., 2005.
- [21] GEANT4 collaboration, *GEANT*, Nucl. Inst. and Methods, A 506 (250), 2003.
- [22] Boole, LHCb simulation software. For details, see <http://lhcb-comp.web.cern.ch/lhcb-comp/Digitization/relatedNotes.html>
- [23] Corti, G., et al., *Software for the LHCb Experiment*, IEEE Transactions on Nuclear Science, 53 (3), 2006.
- [24] Peter Weidenkaff, "Study of $D^0 - \bar{D}^0$ mixing with the LHCb detector" (Diploma Thesis), 2010.
<http://www.physi.uni-heidelberg.de/Publications/D0mixing-weidenkaff.pdf>
- [25] Benayoun, M ; Jones, C, "RICH Reconstruction and Particle Identification Using Ring Fit Methods : Application to the RICH2 Detector", CERN-LHCb-2004-057
- [26] W. Verkerke and D.P. Kirkby, "The RooFit toolkit for data modeling," In the Proceedings of 2003 Conference for Computing in High-Energy and Nuclear Physics (CHEP 03), La Jolla, California, 24-28 Mar 2003, pp MOLT007, [arXiv:physics/0306116].

-
- [27] J. Gaiser, "Charmonium Spectroscopy from Radiative Decays of the J/Ψ and Ψ -Prime", SLAC-R-255
- [28] The LHCb Collaboration, "Time integrated ratio of wrong-sign to right-sign $D^0 \rightarrow K\pi$ decays in 2010 data at LHCb", CERN-LHCb-CONF-2011-029, 2011.
- [29] Sebastian Bachmann, private communication
- [30] Heavy Flavor Averaging Group, http://www.slac.stanford.edu/xorg/hfag/charm/CHARM10/results_mix+cpv.html, 2011.
- [31] S. Bachmann, M. Bessner, J.Marks, U.Uwer, "Time-Dependent Analysis of $WS D^0 \rightarrow K\pi$ Decays", LHCb Analysis Note in preparation.

Acknowledgments

Ich möchte mich bei allen bedanken, die zum Entstehen dieser Arbeit beigetragen haben. Dies sind insbesondere:

- Herr Prof. Uwer als Betreuer meiner Diplomarbeit, der auch immer wieder gute Anregungen zur Analyse hatte
- Herr Prof. Herrmann, der sich als Zweitkorrektor zur Verfügung gestellt hat
- Jörg Marks und Sebastian Bachmann, die das ganze Jahr mit mir zusammengearbeitet haben
- Alexander Bien, Marco Meißner und Sascha Stahl als Bürokollegen, die oft bei Problemen weiterhelfen konnten
- Peter Weidenkaff und Katharina Kreplin, die in ihren Diplomarbeiten einiges erarbeitet hatten, auf das ich aufbauen konnte.
- Die gesamte LHCb-Gruppe in Heidelberg
- Die LHCb-Kollaboration
- Meine Familie
- Und alle, die ich an dieser Stelle vergessen habe

Erklärung

Ich versichere, dass ich diese Arbeit selbstständig verfasst und keine anderen als die angegebenen Quellen und Hilfsmittel benutzt habe.

Heidelberg, den 10. Februar 2012
